



# Activating well-defined $\alpha$ -Fe<sub>2</sub>O<sub>3</sub> nanocatalysts by near-surface Mn atom functionality for auto-exhaust soot purification

Peng Zhang<sup>a</sup>, Min Yang<sup>a</sup>, Dawei Han<sup>a</sup>, Xi Liu<sup>b</sup>, Xiaolin Yu<sup>c</sup>, Jing Xiong<sup>a</sup>, Yuanfeng Li<sup>a</sup>, Zhen Zhao<sup>a</sup>, Jian Liu<sup>a</sup>, Yuechang Wei<sup>a,\*</sup>

<sup>a</sup> State Key Laboratory of Heavy Oil Processing, Key Laboratory of Optical Detection Technology for Oil and Gas, College of Science, China University of Petroleum, Beijing 102249, PR China

<sup>b</sup> School of Chemistry and Chemical, In-situ Center for Physical Science, Shanghai Jiao Tong University, Shanghai 200240, PR China

<sup>c</sup> State Key Laboratory for Structural Chemistry of Unstable and Stable Species, Institute of Chemistry, Chinese Academy of Sciences, Beijing 100190, PR China

## ARTICLE INFO

### Keywords:

Atomic co-catalysts  
Hematite  
Intrinsic mechanism  
Near-surface modulation  
Soot oxidation

## ABSTRACT

Herein, the atomically dispersed manganese (Mn) sites on well-defined  $\alpha$ -Fe<sub>2</sub>O<sub>3</sub> nanosheets (Mn<sub>1</sub>-Fe<sub>2</sub>O<sub>3</sub>) were fabricated by a ligand-assisted *in-situ* crystallization method. Single-step surface engineering facilitates the *in-situ* replacement of Fe atoms in near-surface [FeO<sub>6</sub>] octahedra with monodispersed Mn atoms, as well as the preservation of regularly exposed {001} surface. Under different NO<sub>x</sub> concentration (40, 500 and 2000 ppm), Mn<sub>1</sub>-Fe<sub>2</sub>O<sub>3</sub>-10 catalyst presented the superior catalytic performance, whose T<sub>50</sub> values are 455, 388 and 340 °C, respectively. By combining *in-situ* dynamic characterizations and DFT calculations, the surface [MnO<sub>5</sub>] and adjacent [FeO<sub>5</sub>] octahedra cooperatively boost two crucial steps: the dissociation of adsorbed O<sub>2</sub> and the desorption of molecular NO<sub>2</sub>. The greater the amount of molecular NO<sub>2</sub> produced, the higher the efficiency of soot purification via the NO<sub>2</sub>-assisted oxidation mechanism. Insights into the near-surface modulation and structure-activity relationship provide a promising strategy to improve the availability of surface-active sites in future heterogeneous catalysis.

## 1. Introduction

Diesel engines have been widely used in heavy-duty devices and vehicles with its high fuel-efficiency conversion and excellent durability. [1] However, as the emission standards (Euro 6 or China 6) ever-strengthening, considerable challenges still exist regarding the abatement of diesel particulate matter (PM), commonly known as soot, emitted from the diesel exhaust. [2] Soot particles are the mixture of crystalline and amorphous forms of carbon, which are intermingled with polycyclic and long-chain hydrocarbons. [3] Their aerodynamic diameters are usually less than 2.5  $\mu$ m (PM 2.5), which have caused serious respiratory diseases, including lung cancer and chronic obstructive pulmonary disease (COPD). [4] Compared with the internal cleaning techniques and clean oil technologies, the diesel particulate filter coated with specific catalysts (CDPF) is always regarded as an economical and practical after-treatment technology for soot abatement, where the DPF captures the soot particles in the exhaust and then the catalysts boost them into CO<sub>2</sub> via oxidation reaction to achieve the elimination. [5] However, the burning temperature of accumulated soot particles is

above 550 °C, which is much higher than that of diesel exhaust (200–400 °C). In order to achieve continuous and efficient removal of soot particles, tremendous advance has been contributed on pure oxides, perovskites, spinel oxides, hydrotalcite-derived oxides, cerium-based oxides, alkali metal (K, Na, Li, Rb, and Cs) or f-type metal additives (La and Pr), and supported noble metals (Pt, Pd, Au and Ag). [6–10] Owing to the superior activity, supporting noble metals are still the preferred method to improve the catalytic performance of oxides, whose T<sub>50</sub> values can be reduced to roughly 330–340 °C. However, the usage amount of platinum (Pt) and palladium (Pd) in auto-exhaust catalysts exceeds 40% of the global demand amount reported in the *Pgm market report (2022) of Johnson Matthey*, which is a key contributor to the high-cost premium for auto-exhaust after-treatment system. [11] Thus, the development of high-performance non-noble metal oxide catalysts is always a research hotspot.

Catalytic purification of soot (carbon) particles occurs at the triple-face contact among soot particles, catalysts and gaseous reactants (O<sub>2</sub> and NO), where the surface chemistry of solid catalysts is of particular importance, as the contact interface has usually been regarded as the

\* Corresponding author.

E-mail address: [weiyu@cup.edu.cn](mailto:weiyu@cup.edu.cn) (Y. Wei).

<https://doi.org/10.1016/j.apcatb.2022.122077>

Received 13 June 2022; Received in revised form 10 October 2022; Accepted 13 October 2022

Available online 17 October 2022

0926-3373/© 2022 Elsevier B.V. All rights reserved.

active center. [12] Industrially, the contact mode between catalyst and soot particles is usually a loose contact, which leads to a relatively low efficiency of direct oxidation. The NO<sub>2</sub>-assisted oxidation is still one of the most successful methods to achieve the high-efficient elimination of soot particles at low temperature. It is ascribed to the powerful oxidative ability and mobility of NO<sub>2</sub>, whose concentration in the current exhaust is about 400 ppm. [13] Thus, the precise modulation of surface property to boost the adsorption-activation capacity for O<sub>2</sub> and NO are essential for revealing the reaction mechanism and achieving top performance. However, the conventional supports are usually the polycrystalline oxides, whose physical dimensions (morphology, structure, and composition) and surface arrangements (facets) are always non-uniform, making it difficult to obtain the definite near-surface structures. [14] Thus, achieving the precise modulation of the near-surface structure of host metal oxides with non-noble metals to understand the nature of soot oxidation and develop high-efficient non-noble metal catalysts is still a huge challenge.

Hematite ( $\alpha$ -Fe<sub>2</sub>O<sub>3</sub>) is a typical reducible oxide, which is also naturally abundant and thermodynamically stable. [15] With the advantage of surface engineering, various  $\alpha$ -Fe<sub>2</sub>O<sub>3</sub> nanocrystals with specific surface configuration have been elaborately fabricated. [16,17] The preferentially exposed surface not only facilitates to improve the catalytic performance, but also lays a good foundation for near-surface modulation. Among numerous earth-abundant elements, Mn possesses a similar electronic configuration (3d<sup>5</sup>4s<sup>2</sup>) and atomic radius (161 pm) to ferrum (Fe). And, Mn ions in Mn-based oxides have variable valences, presenting superior redox performance during oxidation reaction. [18,19] Thus, it can be a promising strategy to activate intrinsic catalytic performance of  $\alpha$ -Fe<sub>2</sub>O<sub>3</sub> catalyst by precise tailoring its near-surface structure with combining the crystal facet engineering and near-surface Mn atom modulation.

Herein, the single atomic Mn co-catalysts on well-defined  $\alpha$ -Fe<sub>2</sub>O<sub>3</sub> nanosheets (Mn<sub>1</sub>-Fe<sub>2</sub>O<sub>3</sub>) were elaborately prepared by a ligand-assisted in-situ crystallization method and employed for catalytic soot purification. With the benefit of one-step surface engineering, the as-prepared catalysts still retained the  $\alpha$ -Fe<sub>2</sub>O<sub>3</sub>(001) facet after Mn atoms were introduced. In addition, the monodispersed Mn atoms achieve the in-situ substitution of partial Fe atoms in the near-surface [FeO<sub>6</sub>] octahedra with the aid of strong acid environment and the chelation of acetate. The adsorption-activation capacity for gaseous reactants was precisely modulated by the amount of Mn content. Based on multiple characterizations and density functional theory (DFT) calculations, the pivotal role of {001} near-surface structure was clearly unveiled. Insight into near-surface modulation at the atomic level and the fundamental understanding of the structure-activity relationship can pave the way to improve the availability of surface-active sites, and develop the economic and efficient catalysts in thermal heterogeneous catalysis.

## 2. Experimental sections

### 2.1. Catalyst preparation

All chemicals were purchased from Shanghai Macklin Biochemical Co., Ltd without further refining. The synthesis of hexagonal nanosheet  $\alpha$ -Fe<sub>2</sub>O<sub>3</sub> and Mn<sub>1</sub>-Fe<sub>2</sub>O<sub>3</sub>-x catalysts were prepared via a ligand-assisted in-situ crystallization method, [20] whose schema is displayed in Fig. S1. Typically, 1.092 g of FeCl<sub>3</sub>•6 H<sub>2</sub>O (4.0 mmol) and a certain amount of Mn(NO<sub>3</sub>)<sub>2</sub> aqueous solution (50 wt%) was dissolved in to 2.8 mL of HCl aqueous solution with a pH of about 1.3 under vigorously magnetic stirring. Then, 40.0 mL of C<sub>2</sub>H<sub>5</sub>OH (99.5%) was added into above solution after the FeCl<sub>3</sub> dissolved. After stirring for 10 min, 3.2 g of CH<sub>3</sub>COONa was added into above mixture all at once, and stirring was continued for 1 h. Then the mixture was sealed in a 100 mL of Teflon-lined stainless steel autoclave and kept at 180 °C for 16 h. After natural cooling to ambient temperature, the obtained solid products were collected after washing with distilled water and ethanol for five

times. Finally, the samples were dried in a desiccator at 80 °C for 12 h, and then annealed at 550 °C for 4 h. The obtained catalysts were denoted as Mn<sub>1</sub>-Fe<sub>2</sub>O<sub>3</sub>-x catalysts, where “x%” is the molar ratio of Mn to Fe atom in initial feeding.

### 2.2. Catalyst characterization

The crystal phase was determined by powder X-ray diffraction (Shimadzu XRD 6000). Raman spectrums were carried out on inVia Reflex-Renishaw spectrometer under air condition with an excitation wavelength of 532 nm. The actual molar ratio of Mn to Fe atom in as-prepared catalysts were determined by inductively coupled plasma optical emission spectrometry (ICP-OES, PerkinElmer, OPTIMA 7300 V). The X-ray absorption spectra (XAS) of Mn and Fe K-edge were measured at the XRD station of beamline 4B9A of Beijing Synchrotron Radiation Facility (BSRF) in transmission and fluorescence mode. The specific surface area of samples was calculated by N<sub>2</sub> adsorption-desorption isotherms on Micromeritics Tristar II 3020 M system. The morphology and exposed crystal facet were observed by TEM and HRTEM (JEOL JEM LaB<sub>6</sub> 2100 electron microscope, 200 kV). The atomic arrangement was determined by aberration-corrected scanning transmission electron microscope (AC-STEM, HF5000). The elemental constitution and charge were determined by X-ray photoelectron spectroscopy (XPS) experiments, which were performed on PerkinElmer PHI-1600 ESCA spectrometer. The binding energy of C (1 s) peak (BEs=284.8 eV) was chosen as a reference to calibrate other elements. And the redox performance of as-prepared catalysts was tested through temperature-programmed reduction with H<sub>2</sub> (H<sub>2</sub>-TPR). Besides, temperature-programmed oxidation of NO (NO-TPO) were also carried out, whose results can be supplement for the catalytic performance. In order to intuitively track the dynamic exchange between gaseous O<sub>2</sub> and surface oxygen, 6-pulse isotopic <sup>18</sup>O<sub>2</sub> exchange experiments were carried out at 300, 350 and 400 °C. The injection value of Loop is 0.5 mL, and the gas composition was monitored with mass spectrometer (Hiden DECRA). In addition, dynamic desorption of NO<sub>x</sub> in the true reaction was also monitored by in-situ diffuse reflection infrared Fourier transform spectroscopy (in-situ DRIFTS). Typically, the samples were pretreated with N<sub>2</sub> at 300 °C for 30 min and then cooled to ambient temperature. After subtracting the background under the N<sub>2</sub> atmosphere, the gaseous reactant (5% O<sub>2</sub>/0.2% NO/N<sub>2</sub>, 50 mL min<sup>-1</sup>) was introduced and the spectra were recorded at certain temperature for 15 min.

### 2.3. Catalytic activity tests

The performance for catalytic soot oxidation was evaluated by temperature-programmed oxidation of soot (soot-TPO). Typically, 100 mg of the as-prepared catalyst and 10 mg of the model soot (Printex-U) were grinded with an agate mortar for 5 min to form a tight soot-catalyst contact. Then, the mixture was fixed at the constant temperature section of a fixed-bed quartz reactor through two balls of quartz wool and heated in range of 150–700 °C with a ramp rate of 2 °C min<sup>-1</sup>. The reaction gases (50 mL min<sup>-1</sup>) are composed of NO (0.004% or 0.05% or 0.2%), O<sub>2</sub> (5%) and H<sub>2</sub>O (5%) balanced with Ar. Then, the soot particles can be gradually oxidized to CO<sub>x</sub> (CO and CO<sub>2</sub>), which were continuously recorded by an online gas chromatograph (GC 9890B, Shanghai Linghua Instrument Co., Ltd.). According to the obtained data, four indexes were chosen to evaluate the catalytic performance  $T_{10}$ ,  $T_{50}$ ,  $T_{90}$  and  $S_{CO_2}^m$ , in which the temperatures ( $T_{10}$ ,  $T_{50}$  and  $T_{90}$ ) are corresponding to the soot conversion of 10%, 50% and 90%, respectively. The percentage of CO<sub>2</sub> concentration ( $C_{CO_2}$ ) in all outlet CO<sub>x</sub> concentration is designated as  $S_{CO_2}$ , whose equation is  $S_{CO_2} = 100\% \cdot C_{CO_2} / (C_{CO} + C_{CO_2})$ . And the  $S_{CO_2}^m$  is the  $S_{CO_2}$  while the maximum  $C_{CO_2}$  value is reached.

Turnover frequency (TOF) can reflect the intrinsic activity of catalyst, which is the direct evidence to discriminate the true active sites of as-prepared catalysts. Here, the ratio of reaction rate ( $R_w$ ) to the amount of active oxygen (O\* amount) is defined as the TOF, which was



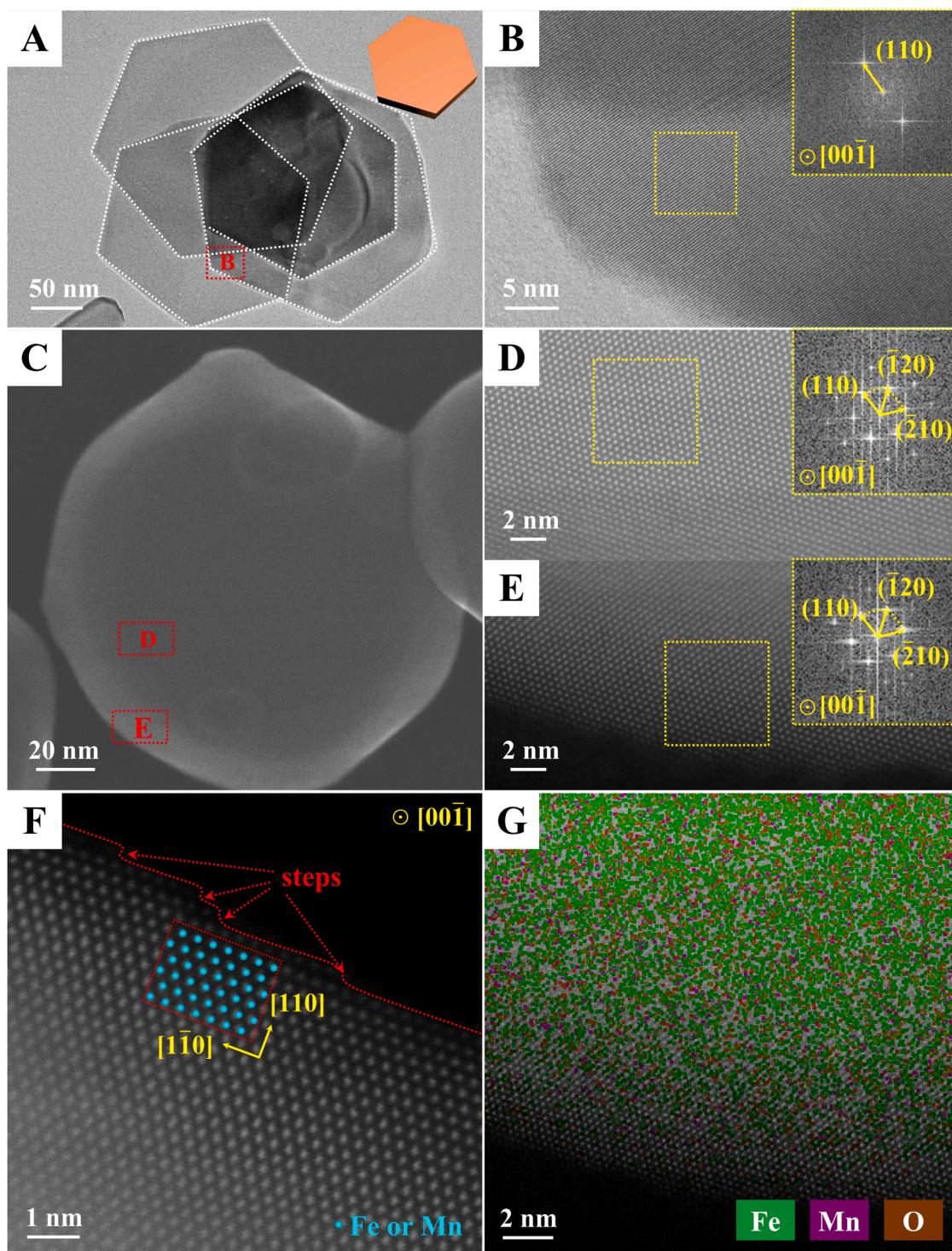


**Fig. 1.** (A,B) TEM and HRTEM images of  $\alpha$ -Fe<sub>2</sub>O<sub>3</sub> catalysts; (C-G) AC-STEM images and EDX elemental maps of as-obtained Mn<sub>1</sub>-Fe<sub>2</sub>O<sub>3</sub>-10 catalyst viewed along the [00-1] zone axis.

determined via isothermal reactions of 270 °C carried out at almost kinetic regime. And the  $R$  values ( $\mu\text{mol g}^{-1} \text{min}^{-1}$ ) was calculated from the fitted slope of line for cumulated CO<sub>x</sub> amount ( $\mu\text{mol g}^{-1}$ ) verse reactive time (min). The process of determining O\* amount is similar with that of  $R$ , but there is no O<sub>2</sub> involved in the reaction. And the O\* amount ( $\mu\text{mol g}^{-1}$ ) can be indirectly quantified by the yield of cumulated CO<sub>x</sub>. In addition, the apparent activation energy ( $E_a$ ) is also a valuable parameter to estimate the intrinsic activity. Here, the  $E_a$  was calculated through Coats-Redfern integral method [21]. The formula is

$$\ln \left[ -\frac{\ln(1-\alpha)}{T^2} \right] = \ln \left[ \frac{AR_s}{\beta E_a} \left( 1 - \frac{2R_s T}{E_a} \right) \right] - \frac{E_a}{R_s} \frac{1}{T}$$

where  $\alpha$  is the conversion of soot (5%~15%),  $\beta$  is the heating rate ( $2 \text{ K s}^{-1}$ );  $R_s$  is the idea gas constant ( $8.314 \text{ J mol}^{-1} \text{ K}^{-1}$ );  $T$  is the reaction temperature (K). Therefore,  $E_a$  could be calculated from the best fitting line of  $\ln[-T^{-2} \ln(1-\alpha)]$  and  $T^{-1}$ .

## 2.4. Computational details

All DFT calculations were performed with the Vienna ab initio simulation package (VASP) code. [22] The exchange and correlation energy functional was expressed with the GGA-PBE. [23] The energy cutoff was fixed as 400 eV and a  $3 \times 3 \times 1$  MP-point mesh was employed for all calculations. The atomic positions were relaxed until the force on each atom was less than  $0.05 \text{ eV } \text{\AA}^{-1}$ , and the convergence tolerance of the energy was set to be  $10^{-5} \text{ eV}$ . The DFT+U approach was used to describe the localization of the 3d electron of Mn and Fe, in which the values of  $U_{\text{eff}}$  were set to 1.9 and 3.3 eV, respectively. [24] Long-range van der Waals (vdW) interactions were handled by the DFT-D3 method. [25] The O-terminated  $\text{Fe}_2\text{O}_3$  {001} surface consisted of c ( $2 \times 2$ ) six-atomic layer supercells with the bottom four layers fixed. The vacuum space that perpendicular to these surfaces was set to  $15 \text{ \AA}$  to minimize the interaction between distinct slab surfaces. Based on the results of the AC-STEM, EXAFS and previous literature [26],  $\text{Mn}_1\text{-Fe}_2\text{O}_{3-x}$  {001} surface was obtained based on the  $\text{Fe}_2\text{O}_3$  {001} model, where a Fe atom on top site was substituted by a Mn atom. The magnetic order of Fe (MAGMOM=4.262) and Mn (MAGMOM=3.5) atom were considered in initial calculation. [24] In addition, several rounds of deoxygenation tests were performed on both models, and a more realistic reaction surface was obtained (Fig. S2).

Reaction transition states (TS) were calculated with the climbing image nudged elastic band (CI-NEB) method. [27] Frequency analysis was carried out to ensure that there was only a single imaginary frequency for the transition state. The energy barrier ( $E_{\text{TS}}$ ) was defined as the total energy difference between the transition state and the initial structure. Moreover, the Gibbs free energy of the species involved in NO oxidation is defined as  $\Delta G = \Delta E + \Delta E_{\text{ZPE}} - T\Delta S$ , where  $\Delta E$ ,  $\Delta E_{\text{ZPE}}$  and  $\Delta S$  denote the calculated electronic energy difference between reactants and products of reactions, the zero-point energy correction and the vibrational entropy at 573.15 K, respectively. In addition, the projected density of state (pDOS), projected crystal orbital Hamilton population (pCOHP) and Bader charge analysis was also used to estimate the charges of surface atoms.

## 3. Results and discussions

### 3.1. Morphology and texture structure of $\text{Mn}_1\text{-Fe}_2\text{O}_{3-x}$ catalysts

As illustrated in Fig. S1, during the nucleation and growth of  $\alpha\text{-Fe}_2\text{O}_3$  nanocrystals, alcohol molecules can combine with the surface  $\text{Fe}^{3+}$  atoms on {001} facet via excellent nucleophilic affinity of oxygen atoms. In addition, with the benefit of strong chelating ability for transition metal ions, the carboxylic anions can also coordinate with both the surface  $\text{Fe}^{3+}$  ions on {001} facet and the  $\text{Mn}^{2+}$  ions in the solution. Thereby, the vertical growth of  $\alpha\text{-Fe}_2\text{O}_3$  nanocrystals along the [001] direction is confined, but the radial one perpendicular to the [001] direction is enhanced. However, the radial growth perpendicular to the [001] direction can also be retarded by the addition of water. Thus, hexagonal  $\alpha\text{-Fe}_2\text{O}_3$  nanosheets with mainly exposed {001} facet can be elaborately synthesized. Meanwhile, Mn ions were also introduced into  $\alpha\text{-Fe}_2\text{O}_3$  lattice with the aid of the chelation of carboxylic anions. Based on the results of ICP-OES and XPS, the surface Mn/Fe atomic ratios are higher than their actual ratios, implying that the near-surface structures of  $\alpha\text{-Fe}_2\text{O}_3$  catalysts have been successfully modulated by Mn atoms (Fig. S3). As can be seen in Fig. 1A, TEM images of  $\alpha\text{-Fe}_2\text{O}_3$  catalyst demonstrate a morphology of uniformly hexagonal nanosheets, whose side length and thickness are ca. 120 and 25 nm, respectively. A clear lattice fringe of  $2.51 \text{ \AA}$  is observed in Fig. 1B along [00-1] zone axis, ascribing to the {110} facet of  $\alpha\text{-Fe}_2\text{O}_3$ . Thus, the hexagonal  $\alpha\text{-Fe}_2\text{O}_3$  nanosheets expose the {001} facets on the top (or bottom) and {110} facets on the sides, where the mainly exposed {001} facet plays a dominant role in catalytic performance. [26] With the increase of Mn ions in  $\text{Mn}_1\text{-Fe}_2\text{O}_{3-x}$  catalysts, the morphology changes into circle

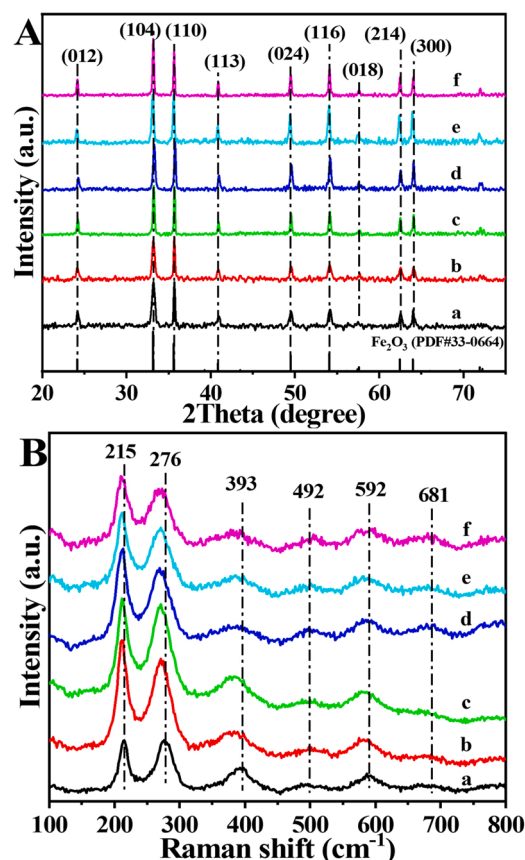
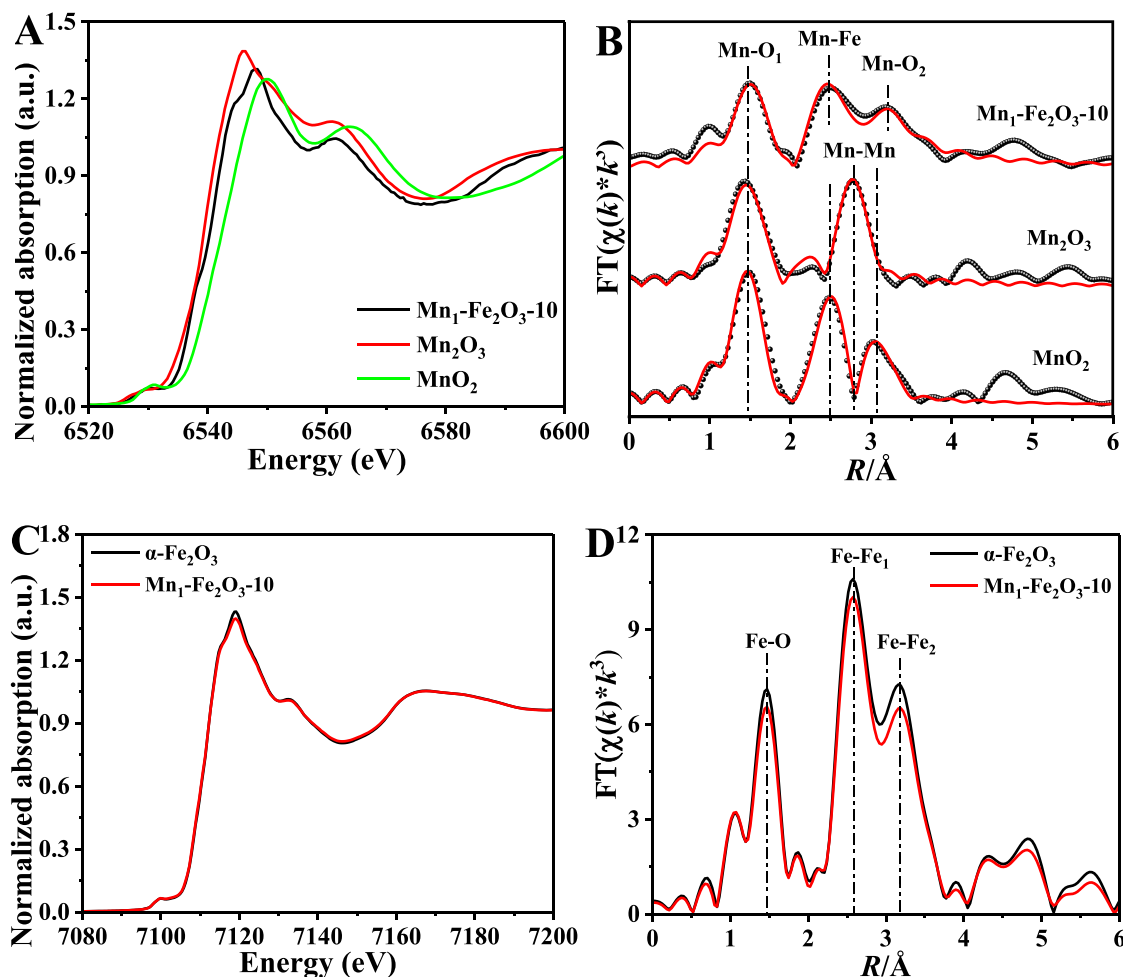


Fig. 2. (A) XRD patterns and (B) Raman spectra of  $\text{Mn}_1\text{-Fe}_2\text{O}_{3-x}$  catalyst: (a)  $\alpha\text{-Fe}_2\text{O}_3$ , (b)  $\text{Mn}_1\text{-Fe}_2\text{O}_{3-3}$ , (c)  $\text{Mn}_1\text{-Fe}_2\text{O}_{3-5}$ , (d)  $\text{Mn}_1\text{-Fe}_2\text{O}_{3-7}$ , (e)  $\text{Mn}_1\text{-Fe}_2\text{O}_{3-10}$ , (f)  $\text{Mn}_1\text{-Fe}_2\text{O}_{3-20}$ .

nanosheets (Fig. S4), and even small nanoparticles for  $\text{Mn}_1\text{-Fe}_2\text{O}_{3-20}$  catalyst (Fig. S5), which can be ascribed to the excess consumption of carboxylic anions. However, the  $\text{MnO}_x$  species are not observed on the surface of nanosheets, suggesting that the introduced Mn ions are evenly dispersed in the near-surface lattice of  $\alpha\text{-Fe}_2\text{O}_3$  nanosheets. Thus, the AC-STEM images and the corresponding energy dispersive X-ray (EDX) mapping images were further employed to determine the near-surface atomic arrangement.  $\text{Mn}_1\text{-Fe}_2\text{O}_{3-10}$  catalyst presents identical atomic configuration between the interior (Fig. 1D) and the edge (Fig. 1E), further confirming the uniform dispersion of introduced Mn atoms. Although a step-like surface is observed at the edge of  $\text{Mn}_1\text{-Fe}_2\text{O}_{3-10}$  catalyst, its exact terminating sublayers are well corresponding to the ideal structure of  $\alpha\text{-Fe}_2\text{O}_3$  {110} facet (Fig. 1F). The high-resolution EDX maps (Fig. 1G) finally prove that the Mn atoms are singly dispersed within the near-surface  $\alpha\text{-Fe}_2\text{O}_3$  lattice. And, the exposed surface of  $\text{Mn}_1\text{-Fe}_2\text{O}_{3-20}$  catalyst with nanoparticle morphology is still  $\alpha\text{-Fe}_2\text{O}_3$  {001} and {110} facets (Fig. S6b), and its similarly step-like surface without lattice deformation is also observed (Fig. S6c), where Mn, Fe and O elements are evenly distributed (Fig. S6d). As a result, the introduced Mn atoms are monodispersed and successfully replace partial Fe atoms in near-surface  $[\text{FeO}_6]$  octahedra.

XRD patterns (Fig. 2A) demonstrate that all as-prepared catalysts are rhombohedral  $\alpha\text{-Fe}_2\text{O}_3$  phase with a space group of  $R_{3c}$  (JCPDS 33-0664). [28] The diffraction peaks corresponding to  $\text{MnO}_x$  (i.e.,  $\text{Mn}_2\text{O}_3$  or  $\text{MnO}_2$ ) are absent, eliminating the segregation of Mn atoms during the preparation. The expansion of lattice parameters and the increase of grain sizes calculated in  $\alpha\text{-Fe}_2\text{O}_3$  nanocrystals jointly confirming that partial Fe atoms were replaced by Mn atoms. (Table S1). Raman spectra also support above results, with the peaks assigned to the  $2A_1g$  (215 and  $393 \text{ cm}^{-1}$ ) and  $3E_g$  (288, 398 and  $605 \text{ cm}^{-1}$ ) vibrational





**Fig. 3.** (A) Mn K-edge XANES spectra, (B) FT  $k^3$ -weighted EXAFS spectra (points) and curvefit (lines) for the Mn K-edge of  $\text{Mn}_2\text{O}_3$ ,  $\text{MnO}_2$  and  $\text{Mn}_1\text{-Fe}_2\text{O}_3\text{-10}$  catalysts; (C) Fe K-edge XANES spectra, (D) FT  $k^3$ -weighted EXAFS spectra for Fe K-edge of  $\text{Mn}_1\text{-Fe}_2\text{O}_3\text{-10}$  and  $\alpha\text{-Fe}_2\text{O}_3$  catalysts.

modes for typical hematite phase (Fig. 2B). [29] With the increase of Mn content, these peaks show a red shift, indicating the weakening of O-M-O bond. There is also a weak Raman peak at around  $681\text{ cm}^{-1}$  corresponding to the O-Mn-O vibration in  $[\text{MnO}_6]$  units. [30] Among them, the Raman peak at  $215\text{ cm}^{-1}$  was chosen as the standard to trace the change of other Raman peaks (marked as  $I_{276}/I_{215}$  and  $I_{681}/I_{215}$ ). As summarized in Table S1, the  $I_{276}/I_{215}$  values of  $\text{Mn}_1\text{-Fe}_2\text{O}_3\text{-x}$  catalysts (0.81–0.95) are lower than that of  $\alpha\text{-Fe}_2\text{O}_3$  (1.00), attributing to the asymmetric vibration of the O-Fe-O bond induced by Mn substitution. The result corresponds well to the conclusion of XRD, and can also be verified by the increasing  $I_{681}/I_{215}$  values (0.08→0.25) with the increase of Mn content. Thereby, both  $\alpha\text{-Fe}_2\text{O}_3$  and  $\text{Mn}_1\text{-Fe}_2\text{O}_3\text{-x}$  catalysts display type-III  $\text{N}_2$  adsorption isotherms with H3 hysteresis loops, which is typically associated with the disorder nanopores created by the accumulation of nanoparticles (Fig. S7). In addition, their specific surface area ( $S_{\text{BET}}$ ) is in range of  $30\text{--}40\text{ m}^2\text{ g}^{-1}$ , and the total pore volume is also in a certain range ( $0.30\text{ cm}^3\text{ g}^{-1}$ ) (Table S1), consistent with TEM and AC-STEM images. In summary, a series of  $\text{Mn}_1\text{-Fe}_2\text{O}_3\text{-x}$  catalysts have been successfully fabricated, of which partial Fe atoms in near-surface  $[\text{FeO}_6]$  units were uniformly substituted by singly dispersed Mn atoms.

### 3.2. Chemical and coordination environment of $\text{Mn}_1\text{-Fe}_2\text{O}_3\text{-x}$ catalysts

XAS measurements were carried out to probe the local coordination environment of Mn atoms. (Fig. 3 and S8) In  $\text{Mn}_1\text{-Fe}_2\text{O}_3\text{-10}$  catalyst, the absorption-edge energy of Mn atoms is between that of  $\text{Mn}_2\text{O}_3$  and  $\text{MnO}_2$ , indicating that the bi-, tri- and tetra-valent Mn ions coexist in

$\text{Mn}_1\text{-Fe}_2\text{O}_3\text{-x}$  catalysts (Fig. 3A). It is further confirmed by the intensity of the white line in X-ray absorption near-edge structure (XANES) spectra. In the Fourier transformed (FT) R-space spectra of Mn K-edge extended X-ray absorption fine structure (EXAFS) spectra,  $\text{Mn}_2\text{O}_3$  sample displays two prominent peaks at  $1.90$  and  $2.89\text{ Å}$ , which are designated to the Mn-O and Mn-Mn<sub>1</sub> scatterings, respectively (Fig. 3B and Table 1). The third scattering path at  $3.09\text{ Å}$  was designated to the Mn-Mn<sub>2</sub> path. As for  $\text{MnO}_2$  sample, there are three apparent peaks located at  $1.89$ ,  $2.89$  and  $3.45\text{ Å}$ , also assigning to Mn-O, Mn-Mn<sub>1</sub> and Mn-Mn<sub>2</sub> bonds, respectively. [31]  $\text{Mn}_1\text{-Fe}_2\text{O}_3\text{-10}$  catalyst also illustrates three scattering paths in the best fit model: a Mn-O<sub>1</sub> scattering path ( $1.95\text{ Å}$ ) with a coordination number of  $4.5 \pm 0.6$ , a Mn-Fe scattering path ( $2.94\text{ Å}$ ) with a coordination number of  $6.1 \pm 1.6$ , and a Mn-O<sub>2</sub> scattering path ( $3.68\text{ Å}$ ) with a coordination number of  $2.3 \pm 1.2$ . The absence of Mn-Mn path and the presence of Mn-Fe path implies that the Mn ions are monodispersed near the surface of  $\text{Mn}_1\text{-Fe}_2\text{O}_3\text{-10}$  catalyst rather than Mn oxides, supporting the results of XRD, Raman and AC-STEM. As illustrated in Fig. 3C, the Fe K-edge XANES spectrum of  $\text{Mn}_1\text{-Fe}_2\text{O}_3\text{-10}$  catalyst presents the same position and intensity of the white line as the  $\alpha\text{-Fe}_2\text{O}_3$  catalyst, indicating the perfect substitution of Mn ions near the surface of host  $\alpha\text{-Fe}_2\text{O}_3$  catalysts. Thereby, the local coordination environment of Fe atoms is essentially same ( $[\text{FeO}_6]$  units) in both catalysts, as shown in the FT R-space spectra of Fe K-edge EXAFS (Fig. 3D).

XPS was performed to trace the valence changes of near-surface elements caused by Mn atom substitution, where three elements (Mn, Fe and O) in  $\text{Mn}_1\text{-Fe}_2\text{O}_3\text{-x}$  catalysts are investigated (Fig. 4). The Mn 2p

**Table 1**

Curvefit parameters<sup>a</sup> for Mn K-edge EXAFS for Mn<sub>1</sub>-Fe<sub>2</sub>O<sub>3-x</sub> catalysts and selected reference materials.

	Shell	R/Å	CN	$\sigma^2/\text{\AA}^2$	$\Delta E_0$ (eV)	R-factor (%)
MnO <sub>2</sub>	Mn-O	1.89 (1)	4.2(5)	0.003(1)	-1.2 (11)	1.603
	Mn-	2.89 (1)	2.9(5)	0.004 (1) <sup>b</sup>		
	Mn <sub>1</sub>	3.45 (2)	2.6(6)			
	Mn <sub>2</sub>	1.90 (1)	4.3(4)	0.005 (1) <sup>b</sup>	-2.8 (12)	
Mn <sub>2</sub> O <sub>3</sub>	Mn-O	2.89 (2)	5.7(9)			1.756
	Mn-	3.09 (1)	2.4(5)			
	Mn <sub>1</sub>	1.95 (0)	4.5(6)	0.004(3)	-1.6 (16)	
	Mn-Fe	2.94 (1)	6.1 (16)	0.008(3)		
Mn <sub>1</sub> -Fe <sub>2</sub> O <sub>3-10</sub>	Mn-O <sub>1</sub>	3.68 (1)	2.3 (12)	0.001(3)		1.844
	Mn-O <sub>2</sub>					

<sup>a</sup>  $S_0^2$  was fixed as 0.85. The data ranges for MnO<sub>2</sub> and Mn<sub>2</sub>O<sub>3</sub> standard reference are  $3 \leq k \leq 12.5 \text{ \AA}^{-1}$ ,  $1 \leq R \leq 3.5 \text{ \AA}$ , which are  $3 \leq k \leq 11 \text{ \AA}^{-1}$ ,  $1 \leq R \leq 4 \text{ \AA}$  for Mn<sub>1</sub>-Fe<sub>2</sub>O<sub>3-10</sub> catalyst. The value in brackets represents the relative error of the last decimal place (eg.  $\pm 0.01$ ). The number of variable parameters for MnO<sub>2</sub> and Mn<sub>2</sub>O<sub>3</sub> standard samples are 9 and 8, out of total 14.95 independent data points, respectively. The number of variable parameters for Mn<sub>1</sub>-Fe<sub>2</sub>O<sub>3-10</sub> catalyst is 10, out of total 15.06 independent data points, respectively.

<sup>b</sup> The values of  $\sigma^2$  in standard sample were constrained to reduce the variables.

spectra display two main peaks located at 653.3 and 641.8 eV, which are attributed to spin-orbits of Mn 2p<sub>1/2</sub> and Mn 2p<sub>3/2</sub>, respectively. In Fig. 4A, the XPS peaks of three Mn species are obtained: Mn<sup>4+</sup> (644.8 and 655.3 eV), Mn<sup>3+</sup> (642.1 and 653.5 eV), and Mn<sup>2+</sup> (640.7 and 651.5 eV) [32,33]. With the increase of Mn content, the percentages of dominant Mn<sup>3+</sup> specie decrease slightly. The presence of Mn<sup>4+</sup> ions is accompanied by the generation of chemisorbed oxygen species (O<sub>2</sub><sup>2-</sup> or O<sup>-</sup>) and the low valance Mn<sup>2+</sup> is correlated with the presence of oxygen vacancies (O<sub>Vs</sub>), which can adsorb molecular O<sub>2</sub>. Thus, the ratio ( $R^c$ ) of Mn<sup>4+</sup>/Mn<sup>2+</sup> was calculated, which increases from 0.108 to 0.755, implying the gradually enhanced oxidation capability. Correspondingly, Fe 2p spectra of Mn<sub>1</sub>-Fe<sub>2</sub>O<sub>3-x</sub> catalysts display two main peaks at 723.9 and 710.1 eV, ascribed to spin-orbits Fe 2p<sub>1/2</sub> and Fe 2p<sub>3/2</sub>, respectively [34]. Both main peaks were deconvoluted into the characteristic Fe<sup>3+</sup> (725.3 and 712.2 eV) and Fe<sup>2+</sup> (723.6 and 710.1 eV) species (Fig. 4B). The other peaks centered at 732.4 and 718.1 eV are designated to Fe<sup>3+</sup> satellite peaks. [35] Generally, the low valance Fe<sup>2+</sup> is correlated with the presence of oxygen vacancies (O<sub>Vs</sub>), which will participate in the electron transfer and oxygen activation. [36] With the increase of Mn content, the percentage of Fe<sup>2+</sup> specie increases to 35.4% (Mn<sub>1</sub>-Fe<sub>2</sub>O<sub>3-20</sub>), suggesting the additional O<sub>Vs</sub> formation. (Table S2) It is further confirmed by the electron paramagnetic resonance (EPR) spectra that Mn<sub>1</sub>-Fe<sub>2</sub>O<sub>3-10</sub> catalyst presents an asymmetric peak at around 2.003 (Fig. S9). Thus, the adsorption-activation ability for oxygen will be enhanced with the increase of O<sub>Vs</sub> and Mn<sup>4+</sup> ions in Mn<sub>1</sub>-Fe<sub>2</sub>O<sub>3-x</sub> catalysts, which can be detected by O 1s spectra. There are three oxygen species: chemisorbed oxygen species O<sub>2</sub> and O<sub>2</sub><sup>2-</sup>, and lattice oxygen species O<sup>2-</sup> in Mn<sub>1</sub>-Fe<sub>2</sub>O<sub>3-x</sub> catalysts, whose binding energies are

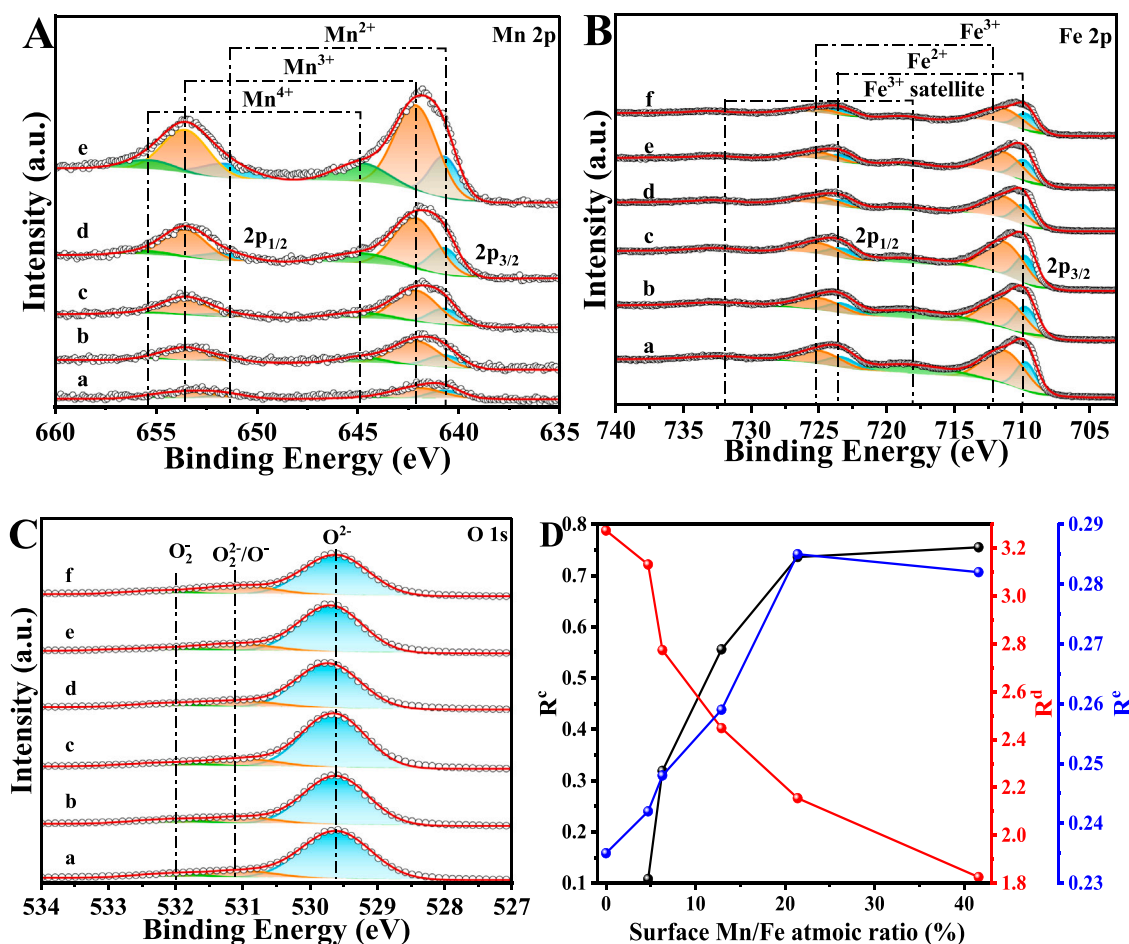


**Fig. 4.** XPS spectra of (A) Mn 2p, (B) Fe 2p and (C) O 1s for Mn<sub>1</sub>-Fe<sub>2</sub>O<sub>3-x</sub> catalysts; (D) correlation between elemental composition and surface Mn/Fe atomic ratio: (a)  $\alpha$ -Fe<sub>2</sub>O<sub>3</sub>, (b) Mn<sub>1</sub>-Fe<sub>2</sub>O<sub>3-3</sub>, (c) Mn<sub>1</sub>-Fe<sub>2</sub>O<sub>3-5</sub>, (d) Mn<sub>1</sub>-Fe<sub>2</sub>O<sub>3-7</sub>, (e) Mn<sub>1</sub>-Fe<sub>2</sub>O<sub>3-10</sub>, (f) Mn<sub>1</sub>-Fe<sub>2</sub>O<sub>3-20</sub>.



**Table 2**

Catalytic performances, reaction rates ( $R_w$ ), density of active oxygen species ( $O^*$  density), TOF and apparent activation energy ( $E_a$ ) values of  $Mn_1-Fe_2O_3-x$  catalysts for soot combustion under loose and tight contact.

	$T_{50}$ ( $^{\circ}C$ )			$S_{CO_2}^m$ (%) <sup>c</sup>	$R_w^d$ ( $\mu mol\ g^{-1}\ min^{-1}$ )	$O^*$ amount <sup>d</sup> ( $\mu mol\ g^{-1}$ )	TOF <sup>e</sup> ( $h^{-1}$ )	$E_a^f$ ( $kJ\ mol^{-1}$ )
	0.004% NO <sup>a</sup>	0.05% NO <sup>b</sup>	0.2% NO <sup>c</sup>					
Soot particles	605	579	567	65.2	—	—	—	185 <sup>g</sup>
$\alpha-Fe_2O_3$	515	487	433	98.2	0.83	75.14	0.663	97.4
$Mn_1-Fe_2O_3-3$	515	479	428	99.0	1.04	83.78	0.744	96.7
$Mn_1-Fe_2O_3-5$	499	456	397	99.3	1.22	122.54	0.597	89.7
$Mn_1-Fe_2O_3-7$	487	421	354	99.5	3.32	150.73	1.322	87.4
$Mn_1-Fe_2O_3-10$	455	388	340	99.6	6.11	206.04	1.779	72.8
$Mn_1-Fe_2O_3-20$	457	394	341	96.0	3.51	186.64	1.128	86.7

<sup>a</sup> Reaction condition: 5%  $O_2$ , 0.004% NO and 5%  $H_2O$  in Ar, 50 mL  $min^{-1}$  (loose contact).

<sup>b</sup> Reaction condition: 5%  $O_2$ , 0.05% NO and 5%  $H_2O$  in Ar, 50 mL  $min^{-1}$  (loose contact).

<sup>c</sup> Reaction condition: 5%  $O_2$ , 0.2% NO and 5%  $H_2O$  in Ar, 50 mL  $min^{-1}$  (tight contact).

<sup>d</sup> Reaction rate at 270  $^{\circ}C$ , 5%  $O_2$  and 0.2% NO in Ar, 50 mL  $min^{-1}$  (tight contact).

<sup>e</sup> The TOF values is obtained by the equation:  $TOF=R/(O^* \text{ amount})$ .

<sup>f</sup>  $E_a$  were by Coats-Redfern integral method.

<sup>g</sup> The  $E_a$  value of pure soot was reported by Cui et al.

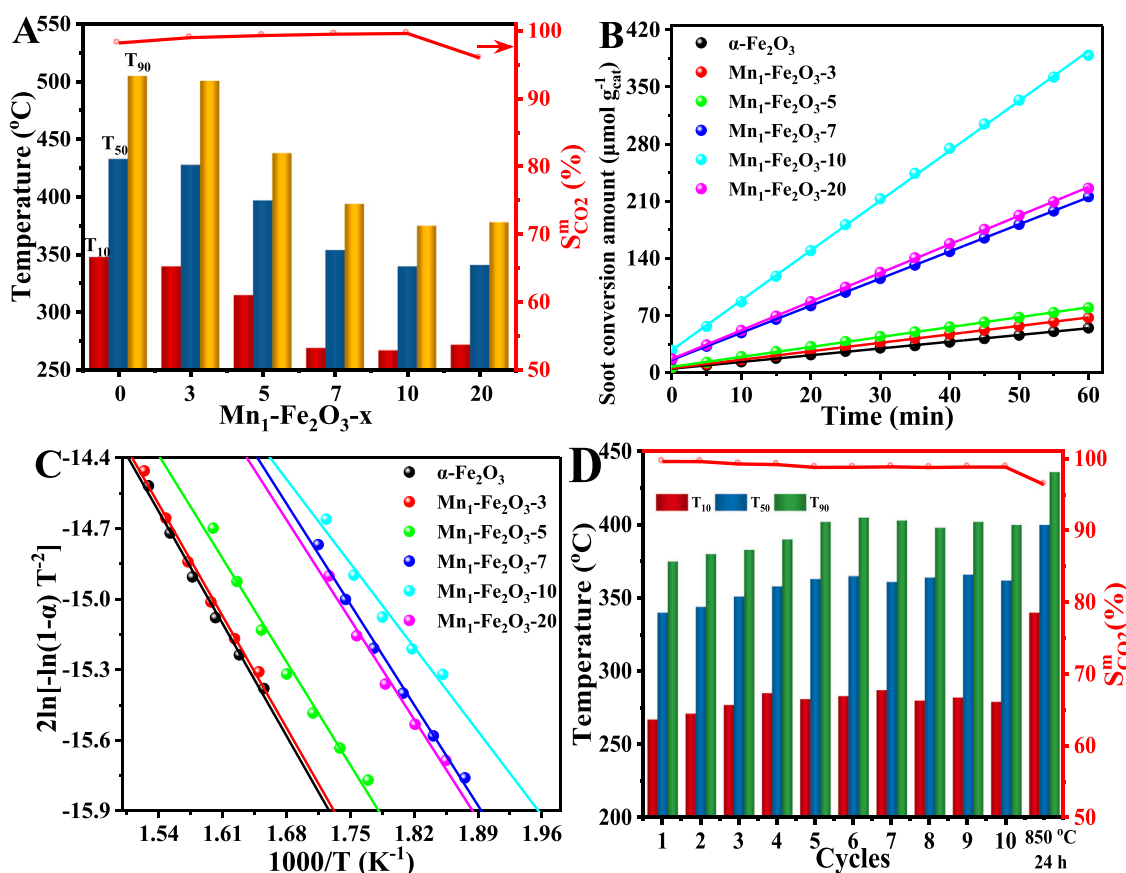


**Fig. 5.** (A) Summary of catalytic activity under tight contact, (B) plots of reaction rate at 290  $^{\circ}C$  and (C) Arrhenius plots of  $2\ln[-T^2 \ln(1-\alpha)]$  vs  $T^{-1}$  at soot conversion of 5–15% over  $Mn_1-Fe_2O_3-x$  catalysts; (D) the cyclic stability of  $Mn_1-Fe_2O_3-10$  catalyst during catalyzing auto-exhaust soot purification.

centered at around 532.0, 531.1 and 529.6 eV, respectively (Fig. 4C). [37] The chemisorbed oxygen species are often considered as the main active oxygen species in the oxidation reaction, whose density will remarkably affect the catalytic performance. Here, it is notable that the ratio ( $R^c$ ) of  $O^{2-}$  ( $O^{2-} + O_2^{2-}$ ) to  $O^{2-}$  shows a maximum value in  $Mn_1-Fe_2O_3-10$  catalyst (0.285) (Fig. 4D and Table S2). Thus,  $Mn_1-Fe_2O_3-10$  catalyst will perform the best oxidation capacity in all as-prepared samples, which is attributed to the superior adsorption-activation ability of gaseous  $O_2$  by optimal  $Mn^{2+}/Mn^{3+}$  and  $Fe^{2+}/Fe^{3+}$  ion pairs.

Considering all the characterizations mentioned above, it can be deduced that monodispersed Mn ions successfully substitute partial  $Fe^{3+}$  ions of near-surface  $[FeO_6]$  octahedra in form of  $Mn^{3+}$  ions. The optimized ratio of  $Mn^{2+}/Mn^{3+}$  and  $Fe^{2+}/Fe^{3+}$  ion pairs near the  $\alpha-Fe_2O_3\{001\}$  surface will prominently boost the generation of active oxygen species, resulting in the super catalytic performance during deep oxidation reaction.

### 3.3. Catalytic activity and durability of $\text{Mn}_1\text{-Fe}_2\text{O}_3\text{-}x$ catalysts for soot oxidation

As summarized in Table 2, the oxidation of pure soot particles is considerably difficult, whose  $T_{50}$  value is above  $567^\circ\text{C}$  and the  $S_{\text{CO}_2}^{\text{m}}$  value is 65.2%, respectively. With the aid of  $\alpha\text{-Fe}_2\text{O}_3$  catalyst, soot particles can be eliminated below  $550^\circ\text{C}$  completely. Besides, the generation of CO is also significantly suppressed ( $S_{\text{CO}_2}^{\text{m}}=98.2\%$ ). Nevertheless, the performance is still not adequate for practical applications, whose exhaust temperature is always in range of  $200\text{--}400^\circ\text{C}$ . As can be seen in Fig. 5A, S10 and S11, the introduced Mn atoms play a positive role in catalytic soot oxidation, whose  $T_{10}$ ,  $T_{50}$  and  $T_{90}$  values decrease remarkably, and the  $S_{\text{CO}_2}^{\text{m}}$  values increase to almost 100%. As summarized in Table 2,  $\text{Mn}_1\text{-Fe}_2\text{O}_3\text{-}10$  catalyst performed the best catalytic activity and selectivity for soot purification among all as-prepared catalysts. The catalytic performance of  $\text{Mn}_1\text{-Fe}_2\text{O}_3\text{-}10$  catalyst under 40 ppm NO and loose contact ( $T_{50}=455^\circ\text{C}$ ) is better than that without NO. The improvement of activity and  $\text{CO}_2$  selectivity are respectively  $32^\circ\text{C}$  and 8.3%, which is attributed to the powerful oxidative ability and mobility of formed  $\text{NO}_2$ . The difference of  $T_{50}$  and  $S_{\text{CO}_2}^{\text{m}}$  values between 40 ppm NO and 500 ppm NO under loose contact is significant, which are  $67^\circ\text{C}$  and 1.4%, respectively. Under different  $\text{NO}_x$  concentration (40, 500 and 2000 ppm),  $\text{Mn}_1\text{-Fe}_2\text{O}_3\text{-}10$  catalyst presented the superior catalytic performance, whose  $T_{50}$  values are 455, 388 and  $340^\circ\text{C}$ , respectively. All  $S_{\text{CO}_2}^{\text{m}}$  values can reach higher than 98%, reducing secondary contamination. As the comparison in Table S3, among the many reported results in the literature, the  $\text{Mn}_1\text{-Fe}_2\text{O}_3\text{-}10$  catalyst exhibited good catalytic performance in soot oxidation. Thus, it can be a promising candidate catalyst for future practical applications.

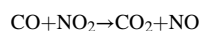
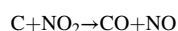
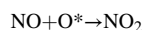
TOF was chosen to accurately reflect the intrinsic performance of the catalyst. Here, the temperature was set at  $270^\circ\text{C}$ , ensuring the reaction take place at the kinetic regime. As illustrated in Fig. 5B and Table 2, the  $R_w$  value of  $\alpha\text{-Fe}_2\text{O}_3$  catalyst is only  $0.83\ \mu\text{mol g}^{-1}\text{ min}^{-1}$ , but increases to  $6.11\ \mu\text{mol g}^{-1}\text{ min}^{-1}$  for  $\text{Mn}_1\text{-Fe}_2\text{O}_3\text{-}10$  catalyst, indicating the highest ignition activity ( $T_{10}=267^\circ\text{C}$ ). Moreover, it presents a similar tendency to the results of soot-TPO, where the  $R_w$  value of  $\text{Mn}_1\text{-Fe}_2\text{O}_3\text{-}20$  catalyst declines to  $3.51\ \mu\text{mol g}^{-1}\text{ min}^{-1}$ , ascribing to the excess enrichment of Mn ions near the surface. The  $\text{O}^*$  amount is also an important factor affecting the intrinsic activity, which was measured by anaerobic titration at  $290^\circ\text{C}$  with the probe molecule of soot particles. Similarly, as shown in Fig. S12 and Table 2,  $\text{Mn}_1\text{-Fe}_2\text{O}_3\text{-}10$  catalyst possesses the maximum  $\text{O}^*$  amount ( $206.04\ \mu\text{mol g}^{-1}$ ). On the basis of above results, TOF was calculated, revealing that  $\text{Mn}_1\text{-Fe}_2\text{O}_3\text{-}10$  catalyst performed the highest intrinsic activity ( $\text{TOF}=1.779\ \text{h}^{-1}$ ), benefiting from the optimal distribution of Mn ions near the  $\alpha\text{-Fe}_2\text{O}_3\{001\}$  surface. Consequently, it presented the best catalytic performance with the lowest  $T_{10}$ ,  $T_{50}$  and  $T_{90}$  values during soot purification.

$E_a$  is another valuable parameter to evaluate the intrinsic activity of the catalysts. Here, the results are calculated from the Arrhenius plots of  $\ln[-T^{-2}\ln(1-\alpha)]$  verse  $T^{-1}$  at 5–15% of soot conversion (Fig. 5C). There is a linear relationship at around 10% of soot conversion, and any linear regression is correlated well with  $R^2$  values over 0.98. As reported by Cui et al., the average value of  $E_a$  value for oxidation of pure soot particles is  $185\ \text{kJ mol}^{-1}$ . [38] With the introduction of as-prepared catalysts, the value of  $E_a$  declined by about  $110\ \text{kJ mol}^{-1}$ , corresponding to their high catalytic performance at low temperature. In Table 2, the  $E_a$  values also illustrated a similar situation to  $T_{10}$  and TOF values that  $\text{Mn}_1\text{-Fe}_2\text{O}_3\text{-}10$  catalyst performed the lowest  $E_a$  value ( $72.8\ \text{kJ mol}^{-1}$ ). In general, the lower the  $E_a$  value is, the easier the reaction proceeds and the faster the frequency of soot conversion. Taking into account the above AC-STEM and XPS results, it can be deduced that the synergistic effect between near-surface Mn and Fe atoms promote the adsorption and activation of gaseous reactants ( $\text{O}_2$  and NO), improving the catalytic performance during auto-exhaust soot oxidation. Thus, the in-situ Mn substitution with an optimal ratio (here is 10%) can enormously enhance the removal efficiency for auto-exhaust soot particles.

The durability of catalysts is an extremely valuable parameter for practical application. As a representative,  $\text{Mn}_1\text{-Fe}_2\text{O}_3\text{-}10$  catalyst was performed on identical soot-TPO cycle tests (Fig. 5D). The catalytic performance ( $T_{10}$ ,  $T_{50}$  and  $T_{90}$  values) of  $\text{Mn}_1\text{-Fe}_2\text{O}_3\text{-}10$  catalyst gradually stabilized after 10 cycles, whose  $T_{10}$ ,  $T_{50}$  and  $T_{90}$  values are 279, 362 and  $400^\circ\text{C}$ , indicating its superior durability for auto-exhaust soot purification. The slight deactivation in former 5 cycles is attributed to the re-stabilization of oxygen vacancies. Large number of malformed  $[\text{MnO}_5]$  octahedra were produced on both the surface and the bulk after in-situ substitution of Mn atoms, forming an unstable initial structure. After the high temperature cycle treatment, the internal oxygen vacancies are replenished due to increased mobility of lattice oxygen and the structure tends to be stable. It is further confirmed by XRD patterns, TEM images and EDX maps. The positions and intensities of diffraction peaks of the used  $\text{Mn}_1\text{-Fe}_2\text{O}_3\text{-}10$  catalyst have not noticeable difference from the fresh counterpart, which still preserved perfect  $\alpha\text{-Fe}_2\text{O}_3$  crystal structure (Fig. S13a). It suggests that a stable structure is generated by the in-situ substitution of Mn ions for near-surface  $\alpha\text{-Fe}_2\text{O}_3$  lattice. The original disc-like nanosheet was also maintained after 5 cycles (Fig. S13b), and its EDX maps (Fig. S13c-g) further confirm the homogeneous distribution of Mn, Fe and O species in the used  $\text{Mn}_1\text{-Fe}_2\text{O}_3\text{-}10$  nanosheets. After the deactivation at  $850^\circ\text{C}$ , the  $T_{50}$  value decreases by  $50^\circ\text{C}$ , attributing to the decrease of optimized surface induced after crystal enlargement and sintering. As the comparison in Table S3,  $\text{Mn}_1\text{-Fe}_2\text{O}_3\text{-}10$  catalyst displays excellent catalytic performance and durability during auto-exhaust soot purification, which can be a promising candidate catalyst for future practical applications.

### 3.4. Molecular-level understanding of the pivotal role of monodispersed Mn ions

Clarifying the reaction path of soot oxidation is the prerequisite for determining the pivotal role of monodispersed Mn ions, which can be classified as the active oxygen mechanism and the  $\text{NO}_2$ -assisted mechanism. [6] As shown in Table 2 and Fig. S11, the catalytic performance of  $\text{Mn}_1\text{-Fe}_2\text{O}_3\text{-}10$  catalyst under 40 ppm NO and loose contact ( $T_{50}=455^\circ\text{C}$ ) is better than that without NO. The improvement of activity and  $\text{CO}_2$  selectivity are respectively  $32^\circ\text{C}$  and 8.3%, which is attributed to the powerful oxidative ability and mobility of formed  $\text{NO}_2$ . In addition, the addition of water also helps to improve the catalytic performance below  $T_{10}$ . It is attributed to the easy dissociation of  $\text{H}_2\text{O}$  on the  $\text{Mn}_1\text{-Fe}_2\text{O}_3\{001\}$  surface, whose energy barrier and dissociative energy is 0.46 and  $-0.05\ \text{eV}$  (Fig. S14). The formed  $\text{HO}^*$  species easily migrates to the surface of soot particles and act as the extra active species to boost its oxidation, supporting the results of literature. [39] Above results demonstrate that the  $\text{NO}_2$ -assisted oxidation plays a dominant role in catalyzing soot removal. The corresponding reactions can be simply summarized as follows:



The high-efficient removal efficiency for soot particles is ultimately attributed to the significant increase in the number of surface-active oxygen species, where  $\text{NO}_2$  is just a powerful medium for the transfer of active oxygen species. The higher the yield of molecular  $\text{NO}_2$ , the better the catalytic performance for soot oxidation via the  $\text{NO}_2$ -assisted oxidation mechanism. Then, extensive in-situ experiments and computational studies were carried out to unveil the inner mechanism and the crucial role of singly dispersed Mn atoms in NO oxidation.

The adsorption-activation capacity for molecular  $\text{O}_2$  is the primary concern in the oxidation reaction, which determines the renewal rate of surface oxygen species, affecting the catalytic performance. [40] Thus, 6-pulse isotopic  $^{18}\text{O}_2$  exchange experiments over  $\alpha\text{-Fe}_2\text{O}_3$  and



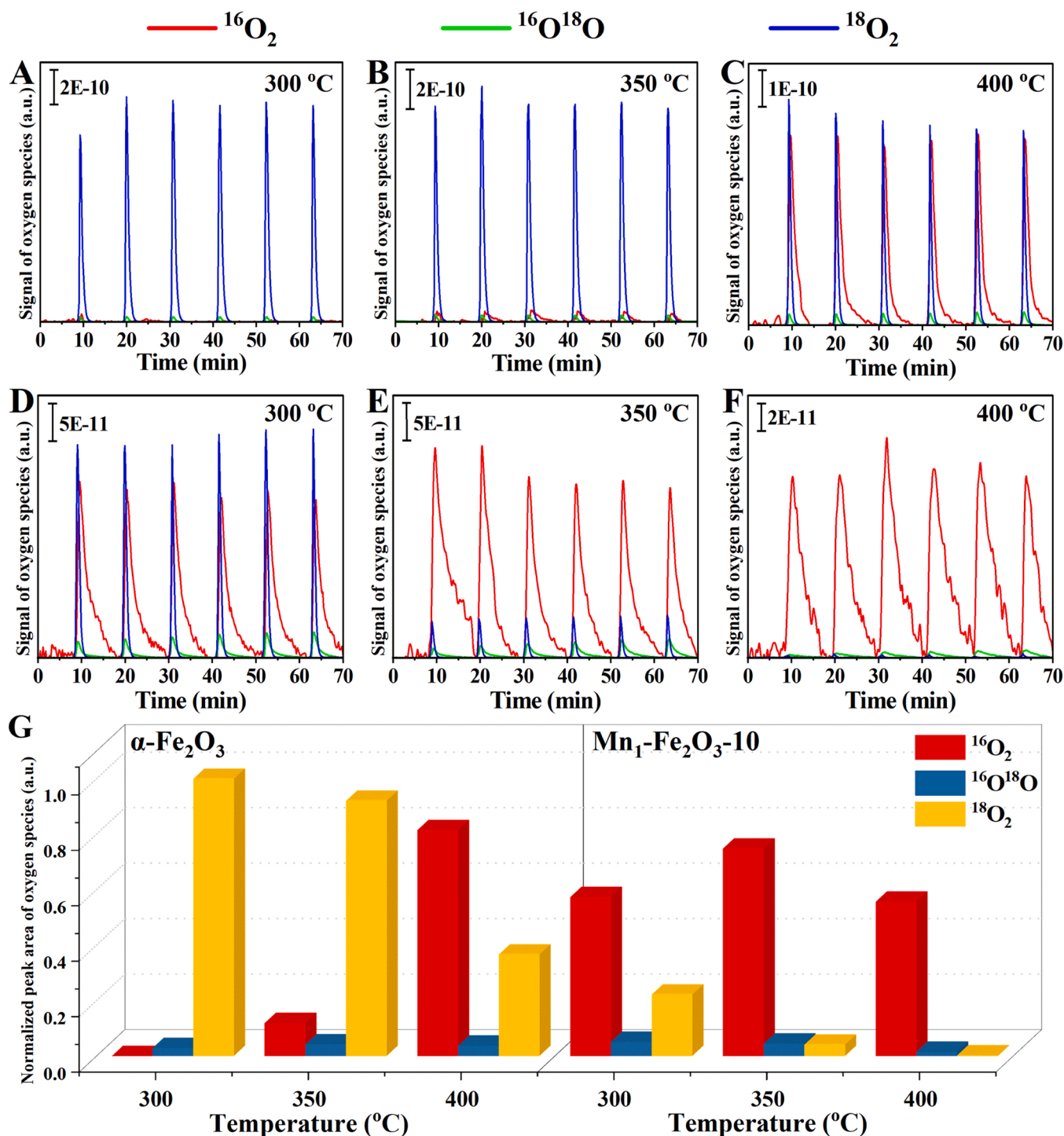


Fig. 6. Isotopic  $\text{O}_2$  production of 6-pulse isotopic  $^{18}\text{O}_2$  exchange experiments over (A-C)  $\alpha\text{-Fe}_2\text{O}_3$  and (D-F)  $\text{Mn}_1\text{-Fe}_2\text{O}_3\text{-10}$  catalysts; (G) the normalized oxygen release of 6-pulse isotopic  $^{18}\text{O}_2$  exchange over  $\alpha\text{-Fe}_2\text{O}_3$  and  $\text{Mn}_1\text{-Fe}_2\text{O}_3\text{-10}$  catalysts at 300, 350 and 400 °C.

$\text{Mn}_1\text{-Fe}_2\text{O}_3\text{-10}$  catalysts were carried out at 300, 350 and 400 °C to intuitively track the dynamic exchange between molecular  $\text{O}_2$  and surface oxygen species (Fig. 6). At 300 °C, the amount of  $^{16}\text{O}_2$  and  $^{16}\text{O}^{18}\text{O}$  over  $\alpha\text{-Fe}_2\text{O}_3$  catalyst is meager compared with that of  $^{18}\text{O}_2$ , implying its poor spillover capability of surface oxygen. Thus, the amount of  $^{18}\text{O}_2$  at this condition is chosen as the standard to normalize other oxygen species. Notably, the amount of  $^{16}\text{O}^{18}\text{O}$  is always low in all 6 separate experiments. And the exchange between molecular  $^{18}\text{O}_2$  and surface  $^{16}\text{O}_2$  displays a dynamic balance, consistent with the  $\text{R}_2$  mechanism ( $^{18}\text{O}_2 + 2\ ^{16}\text{O}_{\text{surf}} \rightarrow ^{16}\text{O}_2 + 2\ ^{18}\text{O}_{\text{surf}}$ ). [41] The oxygen exchange is

significantly affected by the temperature, especially for  $\alpha\text{-Fe}_2\text{O}_3$  catalyst. At 300 and 350 °C, close to the  $T_{10}$  and  $T_{50}$  values mentioned above, the amount of exchanged  $^{16}\text{O}_2$  over  $\text{Mn}_1\text{-Fe}_2\text{O}_3\text{-10}$  catalyst is almost 3 times the  $\alpha\text{-Fe}_2\text{O}_3$  catalyst, implying that the adsorption-activation capacity for molecular  $\text{O}_2$  is enhanced by the Mn ions. Thus, the surface oxygen species can be replenished in time, performing the better redox performance. The result is further proved by  $\text{O}_2\text{-TPD}$  (Fig. S15). The signal is much weaker compared with that of isotopic exchange experiments, implying the weak adsorption of gaseous  $\text{O}_2$ . It is obvious that the spillover capacity of oxygen is improved after introducing Mn ions. And

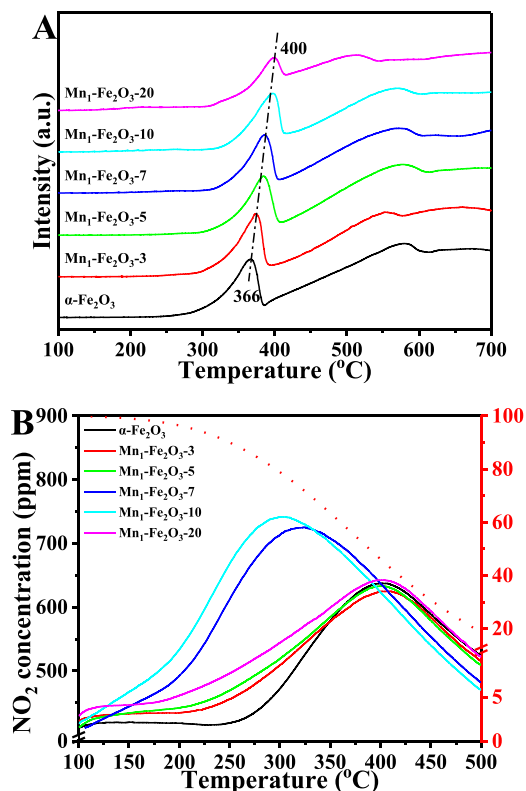


Fig. 7. (A) H<sub>2</sub>-TPR and (B) NO-TPO profiles of Mn<sub>1</sub>-Fe<sub>2</sub>O<sub>3</sub>-x catalysts.

both catalysts present one main desorption peak at 350 °C, ascribing to the surface adsorbed oxygen [41]. Thereby, the decrease of exchanged <sup>16</sup>O<sub>2</sub> at 400 °C over Mn<sub>1</sub>-Fe<sub>2</sub>O<sub>3</sub>-10 catalyst is attributed to the gradual consumption of surface adsorbed oxygen. For  $\alpha$ -Fe<sub>2</sub>O<sub>3</sub> catalyst, the sharp increase of exchanged <sup>16</sup>O<sub>2</sub> at 400 °C is ascribed to the catalyst redox autotuning. Similar results were reported previously in the case of CH<sub>4</sub> oxidation over a cobalt spinel catalyst, where the catalyst changes its redox state by generation of the oxygen vacancies to maintain an equilibrium with the actual chemical potential of the gas phase oxygen [41]. It is further confirmed by H<sub>2</sub>-TPR results, which is displayed in Fig. 7A. There are two main peaks located at 366 and 582 °C over  $\alpha$ -Fe<sub>2</sub>O<sub>3</sub> catalyst, which is ascribed to the step-wise reduction of Fe<sub>2</sub>O<sub>3</sub> to Fe<sub>3</sub>O<sub>4</sub> and Fe<sub>3</sub>O<sub>4</sub> to FeO. [17] With the increase of Mn component, the reduction peak located at 366 °C gradually shifts to high temperature (400 °C). Moreover, there is no apparent reduction peak in range of 100–300 °C, implying the relatively weak adsorption of molecular O<sub>2</sub>. As shown in Fig. S16, the corresponding H<sub>2</sub> consumption over Mn<sub>1</sub>-Fe<sub>2</sub>O<sub>3</sub>-x catalysts (x < 10%) presents inconspicuous difference in range of 100–300 °C, further excluding the absence of MnO<sub>x</sub> species (Mn<sub>2</sub>O<sub>3</sub> or MnO<sub>2</sub>), consistent with the above results of texture structure and local coordination environment. The difference in Mn<sub>1</sub>-Fe<sub>2</sub>O<sub>3</sub>-20 catalyst is attributed to the overabundance of Mn ions on the surface, as supported by its morphology. Consequently, it can be verified by the systematic combination of isotopic <sup>18</sup>O<sub>2</sub> exchange and H<sub>2</sub>-TPR experiments that one of the critical roles of monodispersed Mn ions is to enhance the adsorption and activation of gaseous O<sub>2</sub> over  $\alpha$ -Fe<sub>2</sub>O<sub>3</sub>{001} surface. The relatively strong adsorption ensures the rapid renewal of surface oxygen species in a relatively oxygen-rich environment, presenting the super oxidation capacity.

In-situ DRIFTS and NO-TPO (Fig. 7B) were conducted to assess the dynamic adsorption and desorption of NO<sub>x</sub> species. The peak

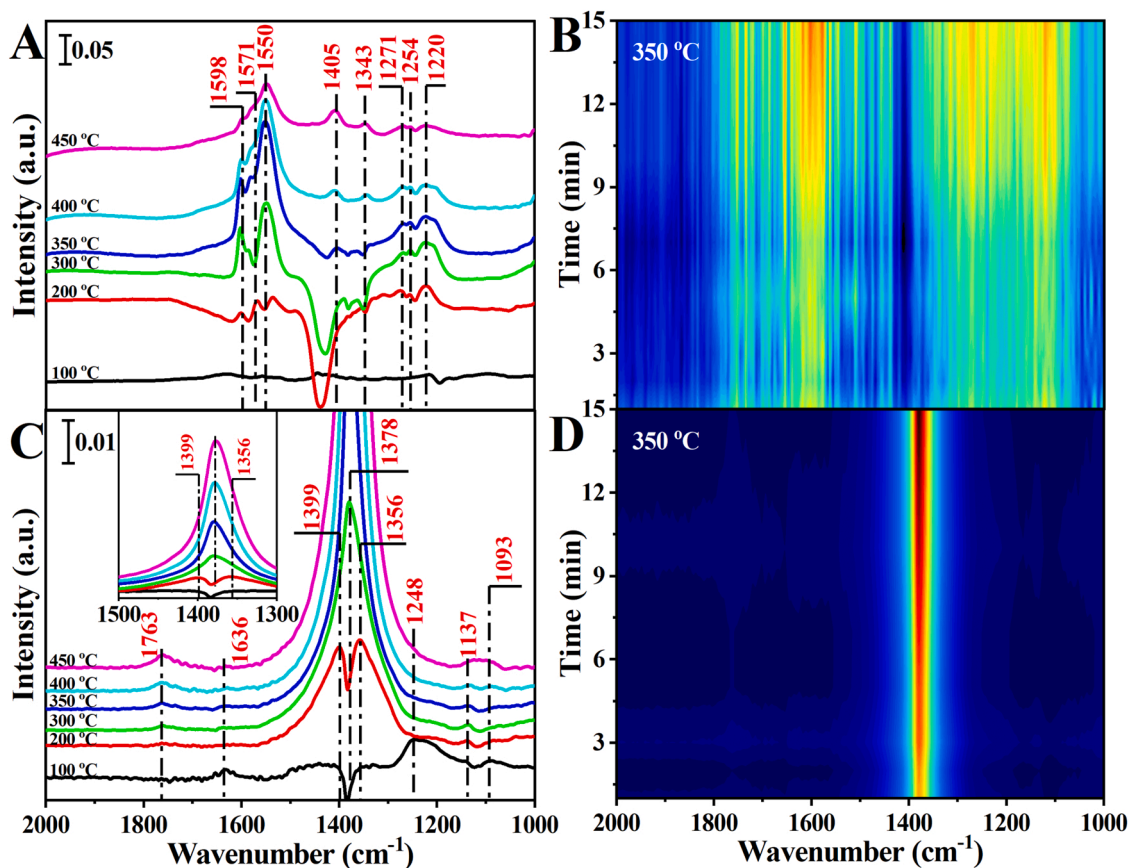


Fig. 8. In-situ DRIFTS of NO<sub>x</sub> dynamic adsorption and desorption over (A,B)  $\alpha$ -Fe<sub>2</sub>O<sub>3</sub> and (C,D) Mn<sub>1</sub>-Fe<sub>2</sub>O<sub>3</sub>-10 catalyst under a 50 mL min<sup>-1</sup> gas flow of 0.2% NO and 5% O<sub>2</sub>.



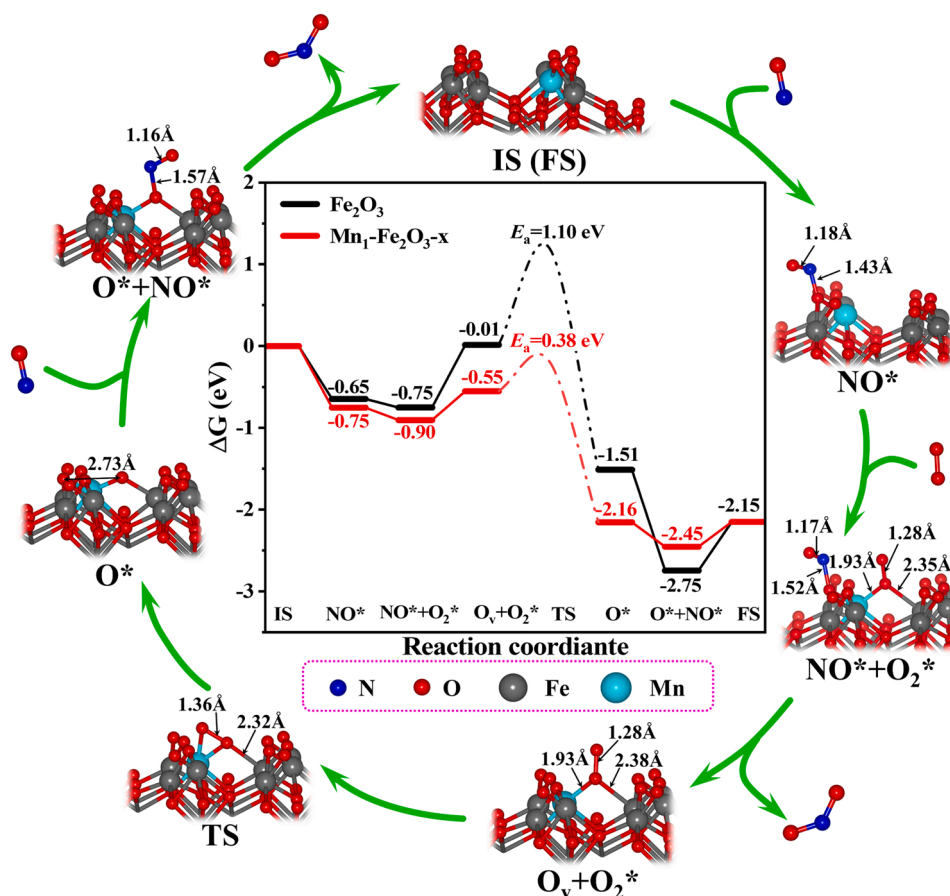


Fig. 9. The calculated free energy diagram and corresponding optimized structures of  $\text{Mn}_1\text{-Fe}_2\text{O}_{3-x}$  catalyst for NO oxidation.

assignments and positions of these  $\text{NO}_x$  species in in-situ DRIFTS are also summarized in Table S4. For  $\alpha\text{-Fe}_2\text{O}_3$  catalyst, the peaks are designated as bridging nitrate ( $1598\text{ cm}^{-1}$ ), bidentate nitrate ( $1571$  and  $1220\text{ cm}^{-1}$ ) and monodentate nitrate ( $1550$ ,  $1271$  and  $1254\text{ cm}^{-1}$ ), respectively (Fig. 8A). [42,43] Apparently, the bridging and bidentate nitrate gradually transforms into monodentate nitrate as the temperature rises and reaches the maximum intensity at  $400\text{ }^\circ\text{C}$ , consistent with the highest yield of molecular  $\text{NO}_2$ . In contrast, the peaks of nitrite species ( $1405$  and  $1343\text{ cm}^{-1}$ ) are weak, implying that NO adsorbed on the surface of  $\alpha\text{-Fe}_2\text{O}_3$  is easily converted to  $\text{NO}_2$ . [44] However, at  $350\text{ }^\circ\text{C}$  (close to above  $T_{50}$  value), the intensity of each  $\text{NO}_x$  species remains virtually unchanged over time (Fig. 8B). It implies that the strong adsorption of NO and  $\text{NO}_2$  coexist on the surface of  $\alpha\text{-Fe}_2\text{O}_3$  catalyst, leading to the relatively low yield of molecular  $\text{NO}_2$  (Fig. 7B). In Fig. 8C, the surface  $\text{NO}_x$  species on  $\text{Mn}_1\text{-Fe}_2\text{O}_{3-10}$  catalyst are mainly in form of nitrites ( $1399$ ,  $1378$  and  $1356\text{ cm}^{-1}$ ), which emerges with the disappearance of free  $\text{NO}_2$  ( $1248\text{ cm}^{-1}$ ). [45] With rising temperature, the stably free  $\text{NO}_2$  species disappear, splitting into two peaks at  $200\text{ }^\circ\text{C}$ , and gradually merging into one peak ( $1378\text{ cm}^{-1}$ ) at  $300\text{ }^\circ\text{C}$  (Fig. S17). In addition, the adsorbed molecular  $\text{NO}_2$  ( $1636\text{ cm}^{-1}$ ) gradually disappears, while a small amount of  $\text{N}_2\text{O}_4$  dimers ( $1763\text{ cm}^{-1}$ ) appears. [46] However, the peaks corresponding to  $\text{NO}_2$  is much weaker compared with that of NO, suggesting that the adsorption of molecular  $\text{NO}_2$  is weakened by introduced Mn ions. Correspondingly, there are only stable nitrite species on the surface of  $\text{Mn}_1\text{-Fe}_2\text{O}_{3-x}$  catalysts at  $350\text{ }^\circ\text{C}$  (Fig. 8D). Thereby, molecular  $\text{NO}_2$  can be produced more efficiently using  $\text{Mn}_1\text{-Fe}_2\text{O}_{3-10}$  catalyst than  $\text{Fe}_2\text{O}_3$  catalyst during NO-TPO tests (Fig. 7B). The excess enrichment of Mn ions suppresses the yield of gaseous  $\text{NO}_2$ , reducing the catalytic efficiency during soot oxidation. Based on the comparison of the aforementioned results of  $\alpha\text{-Fe}_2\text{O}_3$  and  $\text{Mn}_1\text{-Fe}_2\text{O}_{3-10}$  catalysts, it is confirmed that another key role of Mn ions is to weaken the adsorption

of  $\text{NO}_x$ , thus producing more molecular  $\text{NO}_2$  during NO-TPO tests. Additionally, with the combination of the above in-situ DRIFTS results and catalytic performance, it can also be concluded that molecular  $\text{NO}_2$  is the main active species, which catalyzes the oxidation of soot particles rather than surface adsorbed  $\text{NO}_x$  species.  $\text{Mn}_1\text{-Fe}_2\text{O}_{3-10}$  catalyst possesses the optimal configuration of near-surface  $\text{Mn}^{2+}/\text{Mn}^{6+}$  and  $\text{Fe}^{2+}/\text{Fe}^{3+}$  ion pairs, which enormously boosts the renewal of active oxygen species and desorption of molecular  $\text{NO}_2$ , thus presenting the best performance during catalytic soot purification.

### 3.5. Insight into the catalytic reaction mechanism for soot oxidation

DFT calculations were further performed to verify the critical role of Mn atoms and the structure-activity relationship of NO oxidation over the surface of  $\text{Mn}_1\text{-Fe}_2\text{O}_{3-x}$  catalysts. According to the results of EXAFS, the introduced Mn atoms uniformly substitute partial Fe atoms, forming  $[\text{MnO}_5]$  units. In addition, the results of EPR (Fig. S9), isotopic  $^{18}\text{O}_2$  exchange experiments (Fig. 6) and  $\text{O}_2$ -TPD (Fig. S15) confirmed that the spillover capacity of oxygen species was enhanced after introducing Mn ions, boosting the formation of oxygen vacancies. Thus, the real reaction surface at  $300\text{ }^\circ\text{C}$  were established by multiple deoxygenation tests of the ideal model (Fig. S2). As illustrated in Fig. S2e-g, the active Fe atom on  $\alpha\text{-Fe}_2\text{O}_3\{001\}$  facet is  $\text{Fe}_{4c}$  (the coordination number is 4), and the active Mn atom on  $\text{Mn}_1\text{-Fe}_2\text{O}_{3-x}\{001\}$  surface is  $\text{Mn}_{5c}$ , well consistent with above EXAFS results. Then, the Gibbs free energies of  $\text{O}_2$  and NO under single and cooperative adsorption were also calculated. As illustrated in Fig. S18, the adsorption of molecular NO on both slabs is prioritized, which in turn improves the adsorption of molecular  $\text{O}_2$ . In other words, NO and  $\text{O}_2$  tend to co-adsorb on  $\alpha\text{-Fe}_2\text{O}_3$  and  $\text{Mn}_1\text{-Fe}_2\text{O}_{3-x}\{001\}$  facet under reaction conditions.

Based on the results of previous literature [47] and present work, a

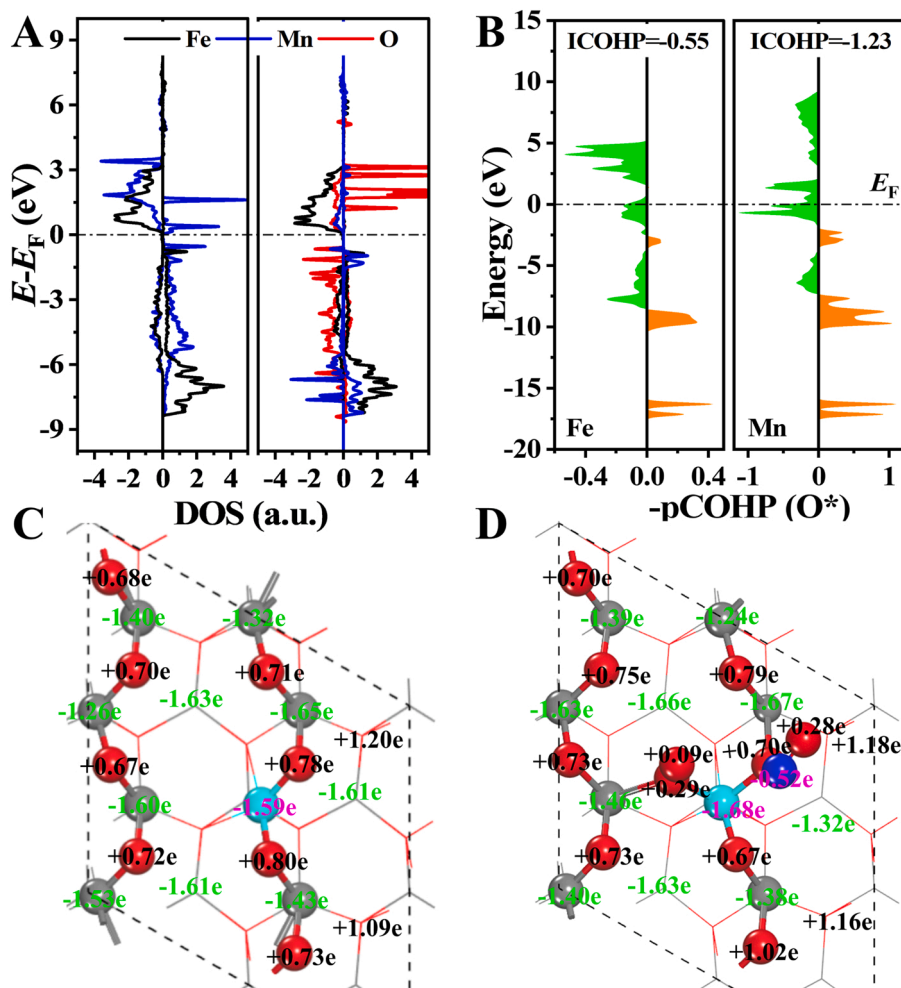


**Fig. 10.** (A) pDOS and (B) pCOHP of Mn<sub>1</sub>-Fe<sub>2</sub>O<sub>3-x</sub> {001} surface with co-adsorbing NO and O<sub>2</sub>, and (C,D) Bader charge numbers of atoms on Mn<sub>1</sub>-Fe<sub>2</sub>O<sub>3-x</sub> {001} facet with and without co-adsorbing NO and O<sub>2</sub>.

hybrid mechanism of MvK and LH are proposed, which consists of six elementary steps (Fig. 9 and S19). Firstly, molecular NO is captured by the bridged O atoms between surface Mn and Fe atoms with a Gibbs free energy ( $\Delta G$ ) drop of 0.75 eV, which further boosts the adsorption of molecular O<sub>2</sub> with a  $\Delta G$  drop of 0.15 eV. As can be seen from the  $\Delta G$  discrepancy in NO+O<sub>2</sub> + 2 \*  $\rightarrow$  \*NO+\*O<sub>2</sub> step, the changes in the adsorption for O<sub>2</sub> were insignificant after introducing Mn ions, consistent with the results of O<sub>2</sub>-TPD (Fig. S15). Secondly, the formed NO<sub>2</sub> dissociates from the oxygen vacancy with a  $\Delta G$  rise of 0.35 eV, which is much lower than that of  $\alpha$ -Fe<sub>2</sub>O<sub>3</sub> catalyst (0.76 eV). It means that the formed NO<sub>2</sub> molecule will be relatively stable on the surface of  $\alpha$ -Fe<sub>2</sub>O<sub>3</sub> catalyst, which is further confirmed by the stable existence of NO<sub>3</sub> species (Fig. S20). The results are well consistent with the aforementioned results of in-situ DRIFTS experiments. Subsequently, the O-O bond of adsorbed O<sub>2</sub> dissociates with the assistance of generated oxygen vacancy (O<sub>V</sub>+\*O<sub>2</sub> $\rightarrow$ \*O), whose energy barrier are 1.10 eV and 0.38 eV for  $\alpha$ -Fe<sub>2</sub>O<sub>3</sub> and Mn<sub>1</sub>-Fe<sub>2</sub>O<sub>3-x</sub> catalysts, respectively. Thus, the surface oxygen species on the Mn<sub>1</sub>-Fe<sub>2</sub>O<sub>3-x</sub> catalysts are relatively easy to replenish under the reaction conditions, accelerating the generation of molecular NO<sub>2</sub>. The results are well consistent with the results of isotopic <sup>18</sup>O<sub>2</sub> exchange experiments (Fig. 6) and NO-TPO (Fig. 7B). Finally, the extra O atom is taken away by another NO molecule through similar steps as described above to return to the initial state (IS or FS). Similarly, the formed NO<sub>2</sub> is relatively challenging to desorb from the surface of  $\alpha$ -Fe<sub>2</sub>O<sub>3</sub> catalyst (0.60 eV). Among all the steps considered, the O<sub>2</sub> dissociation is the kinetic step and needs to be overcome at the

temperatures relevant for NO oxidation, which energy is lower on Mn<sub>1</sub>-Fe<sub>2</sub>O<sub>3</sub> catalyst (0.38 eV) than on  $\alpha$ -Fe<sub>2</sub>O<sub>3</sub> catalyst (1.10 eV). Thus, the generation of molecular NO<sub>2</sub> was substantially promoted with the aid of surface Mn<sub>5c</sub> and adjacent Fe<sub>5c</sub> atoms, further boosting the catalytic performance for soot oxidation.

The pDOS, pCOHP and Bader charge analysis were also employed to reveal the adsorption-activation mechanism from the perspective of electron transfer. After adsorbing O<sub>2</sub>, the DOS of Mn 3d orbital decreases obviously, while that of Fe atom remains almost the same, implying that the Mn atom is the main site for adsorbing and activating O<sub>2</sub> (Fig. 10A). In addition, it is notable that the value of |ICOHP(Mn-O)| (1.23) is higher than that of |ICOHP(Fe-O)| (0.55), where the orange area represents the bond strength and the green area represents the anti-bond strength (Fig. 10B). The high overlap between Mn 3d and O 2p orbits makes it easy for electron transfer from Mn to O atom, boosting the dissociation of O-O bond. Finally, the Bader charge analysis was carried out to quantify the number of transferred electrons. On the one hand, the number of electrons obtained by adjacent O atoms decreases uniformly (0.85e $\rightarrow$ 0.76e) after introducing Mn atoms (Fig. 10C-D). Correspondingly, the adsorbed O<sub>2</sub> gains a charge of 0.38e with the cooperation of surface Mn and adjacent Fe atoms, an increase of 0.11e electrons over singly adsorbed on  $\alpha$ -Fe<sub>2</sub>O<sub>3</sub> catalyst (Fig. S21). Thus, the O-O bond of adsorbed O<sub>2</sub> is easier to dissociate after introducing a proper amount of Mn ions. After NO adsorbs on the surface of Mn<sub>1</sub>-Fe<sub>2</sub>O<sub>3-x</sub> catalysts, the number of electrons obtained by the bridged O atom between surface Mn and Fe atoms presents little difference (0.78e $\rightarrow$ 0.70e), and the



corresponding adsorbed NO loses a charge of 0.24e. For  $\alpha$ -Fe<sub>2</sub>O<sub>3</sub> catalyst, the adsorbed NO loses a charge of 0.06e, while the corresponding bridged O atom acquires extra electrons of 0.27e after adsorption. As O atoms bond with N atoms more closely, NO<sub>2</sub> can more easily exist on the surface of  $\alpha$ -Fe<sub>2</sub>O<sub>3</sub> catalyst. As a result, the critical role of Mn atoms and structure-activity relationship can be elaborately elucidated: the one is to boost the dissociation of O-O bond, accelerating the renewal of active oxygen species; the another is to prompt the desorption of formed NO<sub>2</sub>. Then, Mn<sub>1</sub>-Fe<sub>2</sub>O<sub>3</sub>-10 catalyst can present an enhanced performance during NO oxidation, further improving efficiency of soot oxidation.

#### 4. Conclusions

By the ligand-assisted in-situ crystallization method, the atomic Mn<sub>1</sub>-Fe<sub>2</sub>O<sub>3</sub>-x catalysts have been successfully fabricated, of which the mainly exposed {001} facet was elaborately modulated by single atomic Mn. As indicated by AC-STEM and EXAFS, Mn atoms are dispersed atomically on  $\alpha$ -Fe<sub>2</sub>O<sub>3</sub>{001} surface, and successfully replace partial Fe atoms to form [MnO<sub>5</sub>] octahedra. Additionally, Mn atoms are also enriched near the surface to maintain the host  $\alpha$ -Fe<sub>2</sub>O<sub>3</sub> crystal structure, as confirmed by ICP and XPS. Among as-prepared catalysts, Mn<sub>1</sub>-Fe<sub>2</sub>O<sub>3</sub>-10 catalyst with the optimal ratio of Mn<sup>2+</sup>/Mn<sup>3+</sup> and Fe<sup>2+</sup>/Fe<sup>3+</sup> ion pair presents the best catalytic activity and durability during soot oxidation, whose values of T<sub>50</sub>, S<sub>CO2</sub><sup>m</sup>, TOF and E<sub>a</sub> are 340 °C, 99.6%, 1.779 h<sup>-1</sup> and 72.8 kJ mol<sup>-1</sup>, respectively. By a systematic combination of in-situ experimental analyses and DFT calculations, surface Mn<sub>5c</sub> atoms and adjacent Fe<sub>5c</sub> atoms cooperatively facilitate the dissociation of O-O bond in adsorbed O<sub>2</sub> and the desorption of NO<sub>x</sub> species, thus improving the rapid renewal of surface-active oxygen species and generation of molecular NO<sub>2</sub> under reaction conditions. The higher the yield of molecular NO<sub>2</sub>, the better the catalytic performance for soot oxidation via the NO<sub>2</sub>-assisted oxidation mechanism. The in-depth insight into near-surface modulation at the atomic level provides a promising strategy to precisely improve the availability of surface-active sites via non-noble metals in heterogeneous catalysis.

#### CRediT authorship contribution statement

**Peng Zhang:** Conceptualization, Methodology, Formal analysis, Writing – original draft, Investigation. **Min Yang:** Software, Methodology, Formal analysis. **Dawei Han:** Investigation, Data curation. **Prof. Xi Liu:** Investigation, Formal analysis, Data curation. **Prof. Xiaolin Yu:** Investigation, Formal analysis, Data curation. **Ph. D Jing Xiong:** Formal analysis, Investigation. **Yuanfeng Li:** Formal analysis, Visualization. **Prof. Zhen Zhao:** Project administration, Data curation. **Prof. Jian Liu:** Formal analysis, Investigation. **Prof. Yuechang Wei:** Funding acquisition, Conceptualization, Methodology, Investigation, Formal analysis, Writing – review & editing, Supervision.

#### Declaration of Competing Interest

The authors declare that they have no known competing financial interests or personal relationships that could have appeared to influence the work reported in this paper.

#### Data Availability

Data will be made available on request.

#### Acknowledgments

The authors wish to thank the facility support of the 4B9A beamline of Beijing Synchrotron Radiation Facility (BSRF). This work was supported by the National Natural Science Foundation of China (21972166), Beijing Natural Science Foundation (2202045), National Key Research and Development Program of China (2019YFC1907600).

#### Appendix A. Supporting information

Supplementary data associated with this article can be found in the online version at doi:10.1016/j.apcatb.2022.122077.

#### References

- [1] B. Frank, M.E. Schuster, R. Schlögl, D.S. Su, Emission of highly activated soot particulate-the other side of the coin with modern diesel engines, *Angew. Chem. Int. Ed.* 52 (2013) 2673–2677, <https://doi.org/10.1002/anie.201206093>.
- [2] J.P.A. Neef, M. Makkee, J.A. Moulijn, Diesel particulate emission control, *Fuel Process. Technol.* 47 (1996) 1–69, [https://doi.org/10.1016/0378-3820\(96\)01002-8](https://doi.org/10.1016/0378-3820(96)01002-8).
- [3] H. Richter, J.B. Howard, Formation of polycyclic aromatic hydrocarbons and their growth to soot-a review of chemical reaction pathways, *Prog. Energy Combust. Sci.* 26 (2002) 565–608, [https://doi.org/10.1016/S0360-1285\(00\)00009-5](https://doi.org/10.1016/S0360-1285(00)00009-5).
- [4] H. Li, X. Qian, Q. Wang, Heavy metals in atmospheric particulate matter: a comprehensive understanding is needed for monitoring and risk mitigation, *Environ. Sci. Technol.* 47 (2013) 13210–13211, <https://doi.org/10.1021/es404751a>.
- [5] T.V. Johnson, Diesel emission control in review, *SAE Int. J. Fuels Lubr.* 2 (2001) 1–12, <https://doi.org/10.4271/2009-01-0121>.
- [6] A. Bueno-López, Diesel soot combustion ceria catalysts, *Appl. Catal. B* 146 (2014) 1–11, <https://doi.org/10.1016/j.apcatb.2013.02.033>.
- [7] C. Peng, D. Yu, L. Wang, X. Yu, Z. Zhao, Recent advances in the preparation and catalytic performance of Mn-based oxide catalysts with special morphologies for the removal of air pollutants, *J. Mater. Chem. A* 9 (2021) 12947–12980, <https://doi.org/10.1039/d1ta00911g>.
- [8] W. Ren, T. Ding, Y. Yang, L. Xing, Q. Cheng, D. Zhao, Z. Zhang, Q. Li, J. Zhang, L. Zheng, Z. Jiang, X. Li, Identifying oxygen activation/oxidation sites for efficient soot combustion over silver catalysts interacted with nanoflower-like hydrothermal-derived CoAlO metal oxides, *ACS Catal.* 9 (2019) 8772–8784, <https://doi.org/10.1021/acscatal.9b01897>.
- [9] T. Jakubek, W. Kaspera, P. Legutko, P. Stelmachowski, A. Kotarba, How to efficiently promote transition metal oxides by alkali towards catalytic soot oxidation, *Top. Catal.* 59 (2016) 1083–1089, <https://doi.org/10.1007/s11244-016-0595-x>.
- [10] L. Chen, J. Zhang, J. Wang, P. Chen, M. Fu, J. Wu, D. Ye, Insight into the improvement effect of nitrogen dopant in Ag/Co<sub>3</sub>O<sub>4</sub> nanocubes for soot oxidation: experimental and theoretical studies, *J. Hazard. Mater.* 420 (2021), 126604, <https://doi.org/10.1016/j.jhazmat.2021.126604>.
- [11] A. Beniya, S. Higashi, Towards dense single-atom catalysts for future automotive applications, *Nat. Catal.* 2 (2019) 590–602, <https://doi.org/10.1038/s41929-019-0282-y>.
- [12] K. Yamazaki, T. Kayama, F. Dong, H. Shinjoh, A mechanistic study on soot oxidation over CeO<sub>2</sub>-Ag catalyst with ‘rice-ball’ morphology, *J. Catal.* 282 (2011) 289–298, <https://doi.org/10.1016/j.jcat.2011.07.001>.
- [13] T. Selli, R. Gioria, A.D. Melas, B. Giechaskiel, F. Forloni, P. Mendoza Villafuerte, J. Demuyne, D. Bosteels, T. Wilkes, O. Simons, P. Recker, V. Lilova, Y. Onishi, M. Steffen, B. Grob, A. Perujo, R. Suarez-Bertoa, Measuring emissions from a demonstrator heavy-duty diesel vehicle under real-world conditions-moving forward to Euro VII, *Catalysts* 12 (2022) 184, <https://doi.org/10.3390/catal12020184>.
- [14] C. Xie, Z. Niu, D. Kim, M. Li, P. Yang, Surface and interface control in nanoparticle catalysis, *Chem. Rev.* 120 (2020) 1184–1249, <https://doi.org/10.1021/acs.chemrev.9b00220>.
- [15] K. Yang, Y. Liu, J. Deng, X. Zhao, J. Yang, Z. Han, Z. Hou, H. Dai, Three-dimensionally ordered mesoporous iron oxide-supported single-atom platinum: highly active catalysts for benzene combustion, *Appl. Catal. B* 244 (2019) 650–659, <https://doi.org/10.1016/j.apcatb.2018.11.077>.
- [16] X. Li, W. Wei, S. Wang, L. Kuai, B. Geng, Single-crystalline  $\alpha$ -Fe<sub>2</sub>O<sub>3</sub> oblique nanoparallelepipeds: High-yield synthesis, growth mechanism and structure enhanced gas-sensing properties, *Nanoscale* 3 (2011) 718–724, <https://doi.org/10.1039/C0NR00617C>.
- [17] H.L. Wang, B.F. Jin, H.B. Wang, N.N. Ma, W. Liu, D. Weng, X.D. Wu, S. Liu, Study of Ag promoted Fe<sub>2</sub>O<sub>3</sub>@CeO<sub>2</sub> as superior soot oxidation catalysts: the role of Fe<sub>2</sub>O<sub>3</sub> crystal plane and tandem oxygen delivery, *Appl. Catal. B* 237 (2018) 251–262, <https://doi.org/10.1016/j.apcatb.2018.05.093>.
- [18] Q. Yu, J. Xiong, Z. Li, X. Mei, P. Zhang, Y. Zhang, Y. Wei, Z. Zhao, J. Liu, Optimal exposed crystal facets of  $\alpha$ -Mn<sub>2</sub>O<sub>3</sub> catalysts with enhancing catalytic performance for soot combustion, *Catal. Today* 376 (2021) 229–238, <https://doi.org/10.1016/j.cattod.2020.05.039>.
- [19] F. Ji, Y. Men, J.G. Wang, Y.L. Sun, Z.D. Wang, B. Zhao, X.T. Tao, G.J. Xu, Promoting diesel soot combustion efficiency by tailoring the shapes and crystal facets of nanoscale Mn<sub>3</sub>O<sub>4</sub>, *Appl. Catal. B* 242 (2019) 227–237, <https://doi.org/10.1016/j.apcatb.2018.09.092>.
- [20] L. Chen, X. Yang, J. Chen, J. Liu, H. Wu, H. Zhan, C. Liang, M. Wu, Continuous shape- and spectroscopy-tuning of hematite nanocrystals, *Inorg. Chem.* 49 (2010) 8411–8420, <https://doi.org/10.1021/ic100919a>.
- [21] J. Tan, Y. Wei, Y. Sun, J. Liu, Z. Zhao, W. Song, J. Li, X. Zhang, Simultaneous removal of NO and soot particulates from diesel engine exhaust by 3DOM Fe–Mn oxide catalysts, *J. Ind. Eng. Chem.* 63 (2018) 84–94, <https://doi.org/10.1016/j.jiec.2018.02.002>.

- [22] G. Kresse, J. Furthmüller, Efficient iterative schemes for ab initio total-energy calculations using a plane-wave basis set, *Phys. Rev. B* 54 (1996) 11169–11186, <https://doi.org/10.1103/PhysRevB.54.11169>.
- [23] G. Kresse, D. Joubert, From ultrasoft pseudopotentials to the projector augmented-wave method, *Phys. Rev. B* 59 (1999) 1758–1775, <https://doi.org/10.1103/PhysRevB.59.1758>.
- [24] L. Cheng, Y. Men, J. Wang, H. Wang, W. An, Y. Wang, Z. Duan, J. Liu, Crystal facet-dependent reactivity of  $\alpha$ -Mn<sub>2</sub>O<sub>3</sub> microcrystalline catalyst for soot combustion, *Appl. Catal. B* 204 (2017) 374–384, <https://doi.org/10.1016/j.apcatb.2016.11.041>.
- [25] S. Grimme, J. Antony, S. Ehrlich, H. Krieg, A consistent and accurate ab initio parametrization of density functional dispersion correction (DFT-D) for the 94 elements H–Pu, *J. Chem. Phys.* 132 (2010), 154104, <https://doi.org/10.1063/1.3382344>.
- [26] W. Qu, X. Liu, J. Chen, Y. Dong, X. Tang, Y. Chen, Single-atom catalysts reveal the dinuclear characteristic of active sites in NO selective reduction with NH<sub>3</sub>, *Nat. Commun.* 11 (2020) 1532, <https://doi.org/10.1038/s41467-020-15261-5>.
- [27] G. Henkelman, B.P. Uberuaga, H. Jónsson, A climbing image nudged elastic band method for finding saddle points and minimum energy paths, *J. Chem. Phys.* 113 (2000) 9901–9904, <https://doi.org/10.1063/1.1329672>.
- [28] Z.W. Wang, S.H. Xie, Y. Feng, P.J. Ma, K. Zheng, E.H. Duan, Y.X. Liu, H.X. Dai, J. G. Deng, Simulated solar light driven photothermal catalytic purification of toluene over iron oxide supported single atom Pt catalyst, *Appl. Catal. B* 298 (2021), 120612, <https://doi.org/10.1016/j.apcatb.2021.120612>.
- [29] X. Hu, J.C. Yu, J. Gong, Fast production of self-assembled hierarchical  $\alpha$ -Fe<sub>2</sub>O<sub>3</sub> nanoarchitectures, *J. Phys. Chem. C* 111 (2007) 11180–11185, <https://doi.org/10.1021/jp073073e>.
- [30] Y. Wang, Y. Zheng, Y. Wang, H. Wang, X. Zhu, Y. Wei, Y. Wang, L. Jiang, Z. Yang, K. Li, Evaluation of Fe substitution in perovskite LaMnO<sub>3</sub> for the production of high purity syngas and hydrogen, *J. Power Sources* 449 (2020), 227505, <https://doi.org/10.1016/j.jpowsour.2019.227505>.
- [31] S.V. Ovsyannikov, A.M. Abakumov, A.A. Tsirlin, W. Schnelle, R. Egoavil, J. Verbeeck, G. VanTendeloo, K.V. Glazyrin, M. Hanfland, L. Dubrovinsky, Perovskite-like Mn<sub>2</sub>O<sub>3</sub>: a Path to new manganites, *Angew. Chem. Int. Ed.* 52 (2013) 1494–1498, <https://doi.org/10.1002/anie.201208553>.
- [32] Y. Yang, D. Zhao, Z. Gao, Y. Tian, T. Ding, J. Zhang, Z. Jiang, X. Li, Interface interaction induced oxygen activation of cactus-like Co<sub>3</sub>O<sub>4</sub>/OMS-2 nanorod catalysts in situ grown on monolithic cordierite for diesel soot combustion, *Appl. Catal. B* 286 (2021), 119932, <https://doi.org/10.1016/j.apcatb.2021.119932>.
- [33] P. Wang, J. Wang, X. An, J. Shi, W. Shangguan, X. Hao, G. Xu, B. Tang, A. Abudula, G. Guan, Generation of abundant defects in Mn–Co mixed oxides by a facile agar-gel method for highly efficient catalysis of total toluene oxidation, *Appl. Catal. B* 282 (2021), 119560, <https://doi.org/10.1016/j.apcatb.2020.119560>.
- [34] Y. Kuwahara, A. Fujibayashi, H. Uehara, K. Mori, H. Yamashita, Catalytic combustion of diesel soot over Fe and Ag-doped manganese oxides: role of heteroatoms in the catalytic performances, *Catal. Sci. Technol.* 8 (2018) 1905–1914, <https://doi.org/10.1039/c8cy00077h>.
- [35] L. Wei, X. Li, J. Mu, X. Wang, S. Fan, Z. Yin, M.O. Tade, S. Liu, Rationally tailored redox properties of a mesoporous Mn–Fe spinel nanostructure for boosting low-temperature selective catalytic reduction of NO<sub>x</sub> with NH<sub>3</sub>, *ACS Sustain. Chem. Eng.* 8 (2020) 17727–17739, <https://doi.org/10.1021/acssuschemeng.0c05862>.
- [36] J. Xiong, Y. Wei, Y. Zhang, P. Zhang, Q. Yu, X. Mei, X. Liu, Z. Zhao, J. Liu, Synergetic effect of K sites and Pt nanoclusters in an ordered hierarchical porous Pt–KMnO<sub>3</sub>/Ce<sub>0.25</sub>Zr<sub>0.75</sub>O<sub>2</sub> catalyst for boosting soot oxidation, *ACS Catal.* 10 (2020) 7123–7135, <https://doi.org/10.1021/acscatal.0c01911>.
- [37] P. Zhang, X. Mei, X. Zhao, J. Xiong, Y. Li, Z. Zhao, Y. Wei, Boosting catalytic purification of soot particles over double perovskite-type La<sub>2–x</sub>K<sub>x</sub>NiCoO<sub>6</sub> catalysts with an ordered macroporous structure, *Environ. Sci. Technol.* 55 (2021) 11245–11254, <https://doi.org/10.1021/acs.est.1c01781>.
- [38] B. Cui, L. Zhou, K. Li, Y.-Q. Liu, D. Wang, Y. Ye, S. Li, Holey Co–Ce oxide nanosheets as a highly efficient catalyst for diesel soot combustion, *Appl. Catal. B* 267 (2020), 118670, <https://doi.org/10.1016/j.apcatb.2020.118670>.
- [39] W.N. Yang, Y. Wang, H.L. Wang, Y.N. Zhang, Y. Peng, J.H. Li, Water accelerates and directly participates soot oxidation: an isotopic study, *Appl. Catal. B* 302 (2022), 120837, <https://doi.org/10.1016/j.apcatb.2021.120837>.
- [40] M. Anpo, G. Costentin, E. Giamello, H. Laron-Pernot, Z. Sojka, Characterisation and reactivity of oxygen species at the surface of metal oxides, *J. Catal.* 393 (2021) 259–280, <https://doi.org/10.1016/j.jcat.2020.10.011>.
- [41] J. Gryboś, M. Fedyna, P. Legutko, B. Leszczyński, J. Janas, A. Wach, J. Szlachetko, X. Yu, A. Kotarba, Z. Zhao, Z. Sojka, Mechanistic insights into oxygen dynamics in soot combustion over cryptomelane catalysts in tight and loose contact modes via <sup>18</sup>O/<sup>16</sup>O isotopic variable composition measurements - a hot ring model of the catalyst operation, *ACS Catal.* 11 (2021) 9530–9546, <https://doi.org/10.1021/acscatal.1c02152>.
- [42] X. Wu, F. Lin, H. Xu, D. Weng, Effects of adsorbed and gaseous NO<sub>x</sub> species on catalytic oxidation of diesel soot with MnO<sub>x</sub>–CeO<sub>2</sub> mixed oxides, *Appl. Catal. B* 96 (2010) 101–109, <https://doi.org/10.1016/j.apcatb.2010.02.006>.
- [43] G. Busca, V. Lorenzelli, Infrared study of the adsorption of nitrogen dioxide, nitric oxide and nitrous oxide on hematite, *J. Catal.* 72 (1982) 303–313, [https://doi.org/10.1016/0021-9517\(81\)90013-0](https://doi.org/10.1016/0021-9517(81)90013-0).
- [44] Y. Xin, L. Cheng, Y. Lv, J. Jia, D. Han, N. Zhang, J. Wang, Z. Zhang, X.-M. Cao, Experimental and theoretical insight into the facet-dependent mechanisms of NO oxidation catalyzed by structurally diverse Mn<sub>2</sub>O<sub>3</sub> nanocrystals, *ACS Catal.* 12 (2022) 397–410, <https://doi.org/10.1021/acscatal.1c04357>.
- [45] P. Chen, F. Dong, M. Ran, J. Li, Synergistic photo-thermal catalytic NO purification of MnO<sub>x</sub>/g-C<sub>3</sub>N<sub>4</sub>: Enhanced performance and reaction mechanism, *Chin. J. Catal.* 39 (2018) 619–629, [https://doi.org/10.1016/S1872-2067\(18\)63029-3](https://doi.org/10.1016/S1872-2067(18)63029-3).
- [46] H. Hu, S. Cai, H. Li, L. Huang, L. Shi, D. Zhang, In situ DRIFTS investigation of the low-temperature reaction mechanism over Mn-doped Co<sub>3</sub>O<sub>4</sub> for the selective catalytic reduction of NO<sub>x</sub> with NH<sub>3</sub>, *J. Phys. Chem. C* 119 (2015) 22924–22933, <https://doi.org/10.1021/acs.jpcc.5b06057>.
- [47] J. Hwang, R.R. Rao, L. Giordano, K. Akkiraju, X.R. Wang, E.J. Crumlin, H. Bluhm, Y. Shao-Horn, Regulating oxygen activity of perovskites to promote NO<sub>x</sub> oxidation and reduction kinetics, *Nat. Catal.* 4 (2021) 663–673, <https://doi.org/10.1038/s41929-021-00656-4>.